Geochronology and metamorphic P-T-X evolution of the Eburnean granulite-facies metapelites of Tidjenouine (Central Hoggar, Algeria): witness of the LATEA metacratonic evolution

Abderrahmane Bendaoud, Khadidja Ouzegane, Gaston Godard, Jean-Paul Liégeois, Jean-Robert Kienast, Olivier Bruguier and Amar Drareni

Geological Society, London, Special Publications 2008; v. 297; p. 111-146
doi:10.1144/SP297.6

Geochronology and metamorphic $P-T-X$ evolution of the Eburnean granulite-facies metapelites of Tidjenouine (Central Hoggar, Algeria): witness of the LATEA metacratonic evolution

ABDERRAHMANE BENDAOUD[1], KHADIDJA OUZEGANE[1], GASTON GODARD[2], JEAN-PAUL LIÉGEOIS[3], JEAN-ROBERT KIENAST[4], OLIVIER BRUGUIER[5] & AMAR DRARENI[1]

[1]*Faculté des Sciences de la Terre, de la Géographie et de l'Aménagement du Territoire, USTHB, BP 32, Dar el Beida 16111, Alger, Algérie (e-mail: abendaoud@gmail.com)*

[2]*Equipe Géobiosphère actuelle et primitive, CNRS IPGP, Université Paris 7-Denis Diderot, 4 place Jussieu, case 89, Paris Cedex 05, France*

[3]*Isotope Geology, Africa Museum, B-3080 Tervuren, Belgium*

[4]*Laboratoire de Géosciences Marines, UFR des Sciences Physiques de la Terre, Université Paris 7-Denis Diderot, UMR 7097, 4 place Jussieu, Tour 14, 5ième Etage Paris Cedex 05, France*

[5]*ISTEEM-CNRS, cc 056, Université de Montpellier II, Place Eugène Bataillon, F-34095 Montpellier, France*

Abstract: Central Hoggar, within the Tuareg shield to the east of the West African craton, is known for its complexity owing to the interplay of the Eburnean and Pan-African orogenies. The Tidjenouine area in the Laouni terrane belongs to the LATEA metacraton and displays spectacular examples of granulite-facies migmatitic metapelites. Here, we present a detailed petrological study coupled with *in situ* U–Pb zircon dating by laser-ablation inductively coupled plasma mass spectrometry (ICP-MS) that allows us to constrain the relative role of the Eburnean and Pan-African orogenies and hence to constrain how the LATEA Eburnean microcontinent has been partly destabilized during the Pan-African orogeny; that is, its metacratonic evolution. These metapelites have recorded different metamorphic stages. A clockwise P–T evolution is demonstrated on the basis of textural relationships, modelling in KFMASH and FMASH systems and thermobarometry. The prograde evolution implies several melting reactions involving the breakdown of biotite and gedrite. Peak metamorphic $P-T$ conditions of 860 ± 50 °C and 7–8 kbar (M_1) were followed by a decrease of pressure to 4.3 ± 1 kbar and of temperature to around 700 °C, associated with the development of migmatites (M_2). After cooling, a third thermal phase at *c*. 650 °C and 3–4 kbar (M_3) occurred. U–Pb zircon laser ablation ICP-MS analysis allows us to date the protolith of the migmatites at 2151 ± 8 Ma, the granulite-facies and migmatitic metamorphisms (M_1–M_2) at 2062 ± 39 Ma and the medium-grade metamorphic assemblage (M_3) at 614 ± 11 Ma. This last event is coeval with the emplacement of large Pan-African granitic batholiths. These data show that the main metamorphic events are Eburnean in age. The Pan-African orogeny, in contrast, is associated mainly with medium-grade metamorphism but also mega-shear zones and granitic batholiths, characterized by a high temperature gradient. This can be considered as typical of a metacratonic evolution.

The Tidjenouine metapelites (Central Hoggar, Fig. 1) show a great diversity of minerals (garnet, biotite, quartz, sillimanite, gedrite, corundum, orthopyroxene, cordierite, spinel, feldspar, plagioclase, ilmenite, rutile) forming different assemblages depending on whole-rock composition and extent of metamorphic transformation. The rocks were involved in a prograde metamorphic evolution followed by decompression. Granulite-facies metamorphism was accompanied by melting favoured by biotite or gedrite dehydration. The successive stages of melting, with a progressively increasing amount of melt escape, produced metapelites with a restitic composition. In these rocks, corundum, spinel and sillimanite crystallized in the most All rich microdomains and orthopyroxene in the

From: ENNIH, N. & LIÉGEOIS, J.-P. (eds) *The Boundaries of the West African Craton.* Geological Society, London, Special Publications, **297**, 111–146.
DOI: 10.1144/SP297.6 0305-8719/08/$15.00

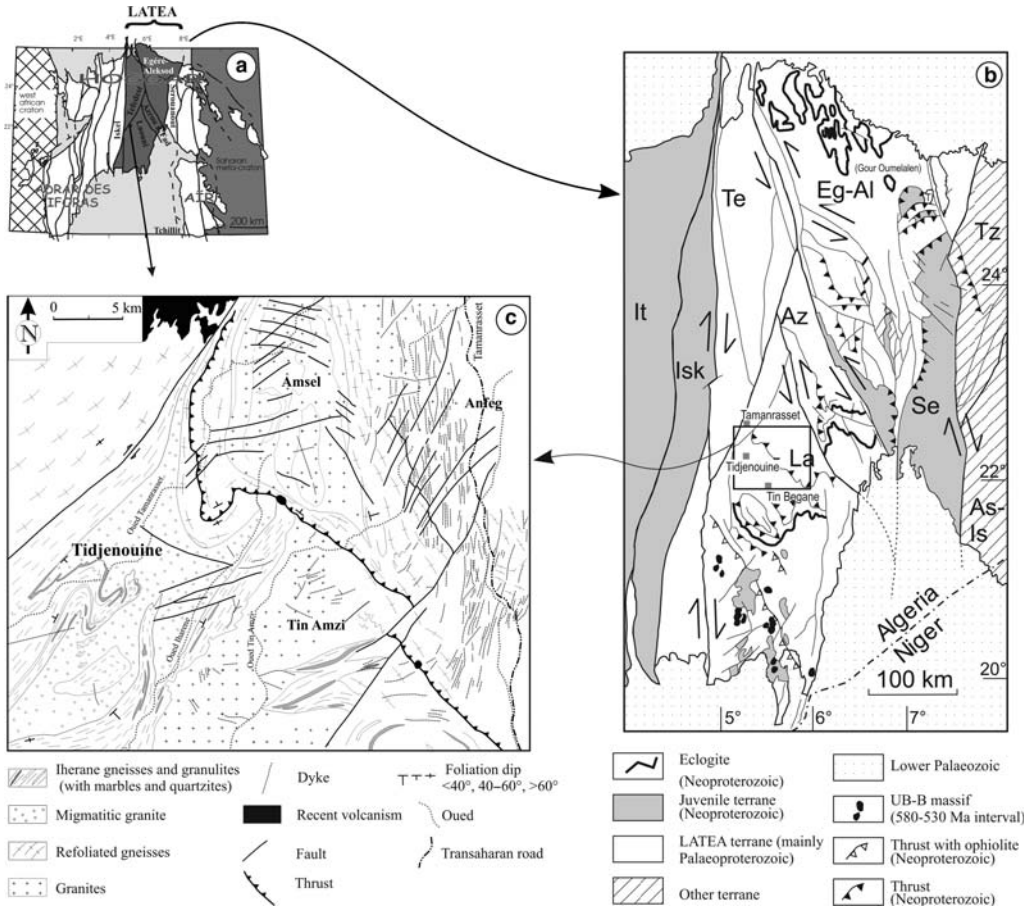

Fig. 1. Geological sketch maps of the Hoggar (**a**, Bertrand *et al.* 1986), of the Tuareg shield (**b**, Black *et al.* 1994) and geological map of the study area (**c**, Liégeois *et al.* 2003). Eg-Al, Egéré–Aleksod; Te, Tefedest; Az, Azrou-n-Fad; Se, Serouenout; Is, Issalane; La, Laouni; Isk, Iskel; It, In Teidini; Tz, Tazat; As-Is, Assodé-Issalane.

most Mg-rich zones. In Central Hoggar, this prograde metamorphism in granulite facies has never been described and the large variability of the metapelite compositions allows us to constrain the P–T–a_{H_2O} evolution.

On the other hand, the Tuareg shield is characterized by the interplay of the Eburnean (*c*. 2 Ga) and the Pan-African (*c*. 0.6 Ga) orogenies. Several terranes of this shield were mostly generated during the Pan-African orogeny (Black *et al.* 1994) whereas others have been only slightly affected, such as the In Ouzzal terrane (Ouzegane *et al.* 2003, and references therein), perfectly preserving ultrahigh-temperature parageneses (Ouzegane & Boumaza 1996; Adjerid *et al.* 2008). The situation of Central Hoggar is much more debated: for some researchers (e.g. Caby 2003), its granulite-facies metamorphism is Pan-African in age (protoliths being mostly Palaeoproterozoic or Archaean); for others, this metamorphism is Eburnean in age, the Pan-African orogeny having generated only high-T greenschist- or amphibolite-facies metamorphism, with high-pressure metamorphism being present only in Neoproterozoic oceanic material thrust on the granulitic basement constituting the LATEA metacraton (Liégeois *et al.* 2003; Peucat *et al.* 2003).

This debate sharply emphasizes the question of how a cratonic basement behaves during an orogeny and how it can be remobilized and what are the consequences of such behaviour. This questions also the nature of the LATEA microcontinent: craton, metacraton or mobile belt? To tackle this problem, this paper focuses on the well-preserved granulites of the Tidjenouine area. It aims at (1) reconstructing the thermotectonic evolution of

these granulites on the basis of detailed mineralogical and paragenetic study of diverse reaction textures preserved in the metapelites; (2) dating the metamorphic assemblages deciphered. For this purpose, a large number of samples of metapelites have been collected and studied. The $P-T$ conditions and $P-T$ path were constrained by using textural relationships, thermobarometry and appropriate petrogenetic grids and $P-T$ pseudosections. The resulting constrained $P-T$ paths, coupled with additional field relationships, allow us to interpret properly the different U–Pb zircon ages provided by laser ablation inductively coupled plasma mass spectrometry (ICP-MS) and by the older conventional U–Pb bulk zircon method. Finally, this allows us to propose a geodynamical evolution of the LATEA microcontinent, highlighting a metacratonic evolution.

Regional geology and lithology

The Tidjenouine area (Central Hoggar, Algeria; Fig. 1) is located in the NW part of the Laouni terrane (Fig. 1b), one of the 23 terranes of the Tuareg shield that were amalgamated during the Pan-African orogeny (Black *et al.* 1994). The Laouni terrane is composed of a granulite- to amphibolite-facies basement separated from Pan-African lithologies by mega-thrusts, such as the Tessalit ophiolitic remnant in the south and the eclogite lenses and associated oceanic material in the Tin Begane area (Liégeois *et al.* 2003). The Laouni terrane is one of the four terranes constituting the LATEA micro-continent (LATEA is an acronym of Laouni, Azrou-n-fad, Tefedest and Egéré-Aleksod terranes; Fig. 1b). According to Liégeois *et al.* (2003), the Archaean and Eburnean LATEA microcontinent was dismembered by mega-shear zones and intruded by granitic batholiths during the main episode of the Pan-African orogeny (640–580 Ma).

The granulite-facies rocks of the Tidjenouine area are composed of two units: (1) migmatitic gneisses with locally recognizable metapelitic and metabasic lenses; (2) migmatitic biotite–garnet–sillimanite metapelites interbanded with olivine–spinel marbles, sillimanite-bearing quartzites and metabasic layers. The quartzites form 100 m thick folded ridges, whereas the marbles occur as boudin alignments, a few metres in thickness. All these rocks are crosscut by Pan-African granites. At contacts between marbles and granites, skarns can be observed. The granulite-facies metamorphism is accompanied by subhorizontal foliations and tangential tectonics.

Few geochronological data are available in the Laouni terrane: these include the following: (1) the Pan-African Anfeg granitic batholith has been dated at 608 ± 7 Ma (U–Pb zircon, Bertrand *et al.* 1986; recalculated by Liégeois *et al.* 2003); (2) the Pan-African amphibolite-facies metamorphism of the thrust oceanic material at Tin Begane has been dated at 685 ± 20 Ma (Sm–Nd mineral isochron; Liégeois *et al.* 2003); (3) a granulite and a migmatitic granite in the Tidjenouine area have been dated to Eburnean ages of 1979 ± 33 Ma and 2038 ± 15 Ma (U–Pb zircon, Bertrand *et al.* 1986; recalculated by Liégeois *et al.* 2003). A migmatite from the neighbouring Azrou n'Fad terrane gave strongly discordant zircons with an upper intercept of 2131 ± 12 Ma and a lower intercept of 609 ± 17 Ma (Barbey *et al.* 1989), thus the age of the migmatitization is ambiguous. The *c.* 2 Ga ages are interpreted either as the age of the protoliths and the granulite-facies metamorphism (Bertrand & Jardim de Sá 1990; Ouzegane *et al.* 2001; Liégeois *et al.* 2003) or as the age of the protoliths, the granulite-facies metamorphism being Pan-African in age (Barbey *et al.* 1989; Caby 2003). Other workers have indicated that they cannot choose between the two hypotheses (Bendaoud *et al.* 2004; Benyahia *et al.* 2005). Three arguments sustain an Eburnean age for the granulite-facies metamorphism: (1) the zircons dated by Bertrand *et al.* (1986) in the Tidjenouine area have not recorded the Pan-African orogeny; (2) in the Gour Oumelalen region (NE LATEA), a series of granulitic rocks have been dated both by the conventional and ion microprobe U–Pb on zircon methods, and an age of *c.* 1.9 Ga has been inferred for the metamorphism without any record of the Pan-African orogeny (Peucat *et al.* 2003); (3) the *c.* 685 Ma old eclogite- and amphibolite-facies oceanic material has not been affected by the granulitic metamorphism. However, this controversial issue must be resolved by a detailed study of the metamorphic phases and by *in situ* zircon dating of key lithologies.

Main characteristics of the Tidjenouine migmatitic granulites

The main Tidjenouine rock type is a medium- to coarse-grained migmatitic orthogneiss made of quartz + K-feldspar + plagioclase + biotite with minor amounts of garnet. The metapelites that will be described in this study are less abundant. In the central part of the area, the orthogneisses are mainly leucomigmatites surrounded by darker migmatitic gneiss. Their silica values range from 66.4 to 76.1 wt% and the $Mg/(Mg + Fe)$ ratio varies between 0.35 and 0.52. Aluminium saturation index (ASI, A/CNK) values between

1.1 and 1.3 indicate strongly peraluminous compositions (Table 1). Most REE patterns (Fig. 2) of these migmatites show pronounced depletion in heavy REE (HREE), which is a characteristic of magmatic suites that have garnet in their source (Hanson 1989). Some samples, however, have flatter HREE patterns. Ba occurs in the 856–1825 ppm range. Sr (334–533 ppm) and Rb

Table 1. *Representative geochemical data for migmatitic gneiss and metapelites from Tidjenouine area*

Rock type:	Type A		Type C	Type D		Migmatitic gneiss		
Sample:	TD 39	TD 60	Tj 58	TD 67	Tj 5	Tj 80	Tj 139	Tj 120
SiO_2	69.88	63.62	43.29	60.4	69.11	66.42	68.96	76.78
TiO_2	0.78	1.13	0.98	1.35	0.87	0.69	0.58	0.06
Al_2O_3	13.68	16.81	25.76	14.68	13.69	16.15	15.62	13.1
FeO*	6.7	6.2	12.1	13.18	6.15	3.63	5.13	1.55
FeO								
Fe_2O_3	7.45	6.89	13.45	14.65	6.84	4.03	5.7	1.73
MnO	0.08	0.08	0.09	0.15	0.16	0.03	0.04	0.05
MgO	2.05	2.06	10.2	6.49	0.84	1.83	3.84	0.47
CaO	0.45	3.68	0.33	1.23	3.2	2.45	0.64	0.56
Na_2O	0.92	3.04	0.3	0.55	2.41	3.72	0.89	2.29
K_2O	2.56	2.18	2.52	0.16	2.09	3.43	1.6	4.84
P_2O_5	0.04	0.51	0.09	0.33	0.25	0.26	0.1	0.12
LOI	1.8		2.88		0.28	0.92	1.97	
Sum	99.69	100	99.89	99.73	99.74	99.93	99.94	100
Cs	0.123		1.77	0.143	1.56	2.06	0.38	0.22
Rb	91.72	92	168	5.67	86.34	116.85	75.5	92.53
Ba	670	912	618	114	1121	855.76	262.64	1825.35
Th	12.35		29.6	0.71	13.53	50.87	13.31	8.74
U	0.71		1.82	0.39	1.12	2.44	1.07	0.63
Ta	0.392		1.21	0.557	1.01	0.39	0.4	0.1
Nb	9.44	15	18.9	11.15	13.04	7.01	9.01	1.36
La	55.35		73	28.87	58.63	142.05	54.67	33.45
Ce	108.8		149	63.28	119.5	261.17	104.18	64.27
Pb	5.66		11.3	2.15	14.3	31.53	5.11	28.72
Pr	11.34		17.1	7.94	13.63	27.76	11	6.77
Sr	102	344	49.2	40	188	334.47	81.74	533.49
Nd	42.25		64.6	32.65	51.24	97.06	38.66	23.84
Sm	7.19		12.9	7.5	10.27	14.42	6.81	4.48
Zr	254	278	336	184	362	693.38	232.33	130.21
Hf	6.05		8.2	4.25	9.46	16.57	5.28	3.6
Eu	1.46		0.729	1.26	1.92	2.08	0.82	1.75
Gd	5.22		9.37	8.13	8.29	8.11	5.33	3.19
Tb	0.79		1.02	1.29	1.3	0.88	0.73	0.39
Dy	4.17		4.82	8.72	6.91	3.21	3.71	2.1
Y	22.4	43	24.8	62.3	42.4	12.67	18.68	16.57
Ho	0.86		0.816	2.32	1.46	0.41	0.58	0.43
Ga	19.5	24	41.8	7.13	20.7	26.9	22.61	13
Er	2.2		2.25	6.37	4.06	1.35	1.5	1.09
Tm	0.39		0.322	1.42	0.55	0.14	0.19	0.16
Yb	2.31		2.18	10.1	4.17	1.11	1.24	1.15
Lu	0.36		0.349	1.74	0.66	0.13	0.14	0.12
Cu	39.6	28	9.9	16.1	29.5	8.66	12.64	5.35
Cd	0.08			0.25	0.23	0.35	0.09	0.1
V	118	103	162	102	50	77.18	71.84	6.19
Zn	50.6	105	231	28.1	69.2	85.32	66.8	17.52
Co	18.9	25	17.3	20.2	13.4	11.3	14.89	2.97
Cr	108	52	137	159	50.5	56.3	87.6	9.85
Ni	53.4	30	66.1	8.98	17.3	29.17	34.68	2.73

LOI, loss on ignition.

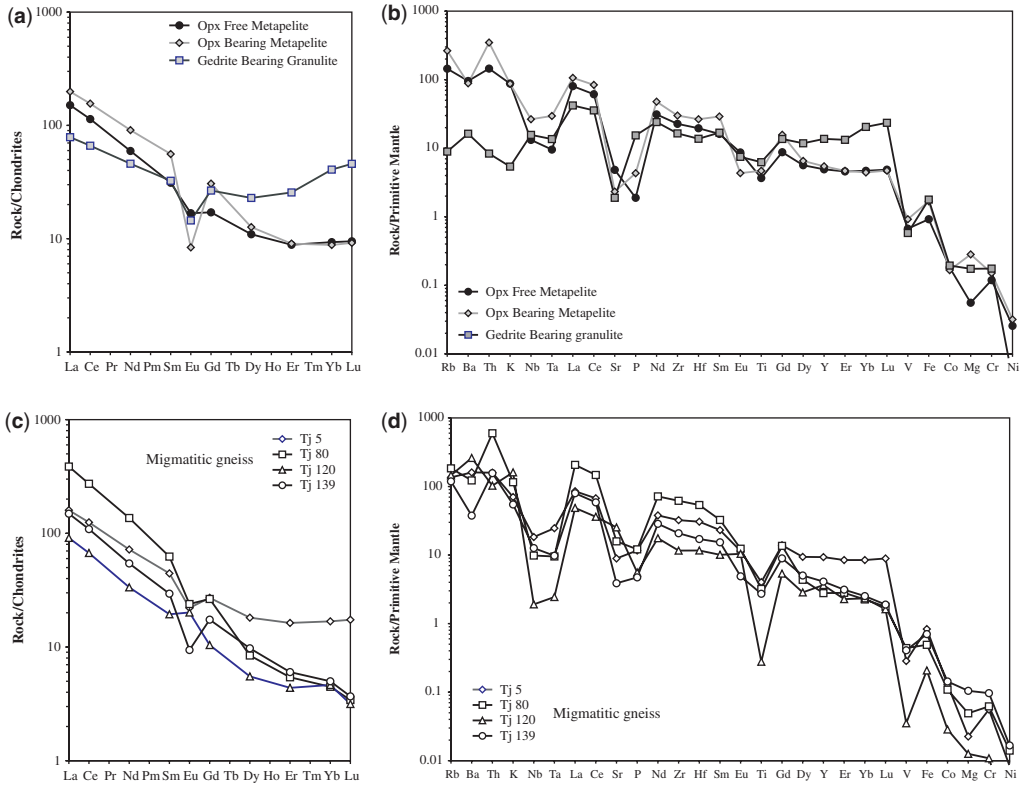

Fig. 2. REE bulk-rock compositions normalized to chondrite (**a**, **c**) and spider diagram normalized to primitive mantle (**b**, **d**) for metapelites (a and b) and migmatitic gneisses (c and d), respectively. Chondrite and primitive mantle normalization values are from Taylor & McLennan (1985) and Sun & McDonough (1989), respectively.

(93–117 ppm) give Rb/Sr values between 0.17 and 1.26. The composition of these rocks suggests that their protoliths resulted from the partial melting of the continental crust, which left a garnet-bearing residue.

The transition from the orthogneiss to the metapelite corresponds to a decrease in the size and abundance of the migmatitic leucosomes, which have a mineralogical composition identical to that of the orthogneiss, until their total disappearance. The orthogneisses can then be considered as sharing the same origin as the leucosomes, but being slightly more allochthonous. This indicates that the felsic intrusions, the granulitic metamorphism and the migmatitization occurred within the same event. Garnet-bearing mafic rocks occur as centimetre- to metre-sized boudins along the granulite-facies foliation within the orthogneiss. Larger bodies (hundreds of metres in size) do not bear garnet. These mafic rocks are not studied here. The garnet-bearing mafic rocks are composed of the Grt–Cpx–Pl–Qtz primary assemblage, which broke down to Opx–Pl during the decompressional stage. On the other hand, the garnet-free mafic rocks with Opx–Cpx–Am–Pl $\pm$ Qtz assemblage are characterized by later destabilization of the amphibole to Opx–Pl, after the decrease of pressure.

The metapelites are migmatitic and dominantly restitic, felsic minerals being commonly less abundant than the mafic ones. A strong layering is observed: Grt–Bt–Sil–Cd-rich restitic layers alternate with Qtz–Pl $\pm$ K-feldspar-rich leucosomes. Migmatitization and dehydration are generally thought to be caused by melting of hydrous phases such as biotite and, less commonly, gedrite. A major feature of the Tidjenouine migmatitic granulites is the presence of well-preserved petrological textures that have developed during prograde metamorphism (e.g. inclusions in garnet or sillimanite), as well as during retrogression (i.e. spectacular symplectites and coronas). This allows an accurate determination of the P–T path evolution.

Different assemblages (Table 2) have been distinguished in the metapelites on the basis of the

Table 2. *Representative mineral assemblages of granulite-facies metapelites from Tidjenouine*

Rock type:	Type A	Type B	Type C	Type D	Type E
Samples:	TD 80–128 TD 63 TD 65 TD 29 TD 39 TD 159	TD 130 TD 134 TD 56	TD 57 TD 57b TD 59	TD 67 TD 67C TD 67A	TD 38
Quartz	X		X	X	X
Biotite	X	X	X		X
Garnet	X	X	X	X	X
Sillimanite	X	X	X	X	
Plagioclase	X		X	X	X
K-feldspar	X	x	x	x	x
Gedrite				X	
Orthopyroxene			X	X	X
Cordierite	X	X	X	X	X
Spinel	X	X	X	X	X
Corundum		X			
Ilmenite	X	X	X	X	X
Rutile	x	X	x	X	
Apatite			x	x	x
Magnetite					x
Graphite	X		X	X	
Pyrite			X		

X, abundant; x, scarce.

presence or absence, depending on the protolith composition, of phases such as orthopyroxene, gedrite, biotite, sillimanite, corundum or quartz. For example, the peak paragenesis of the most Fe-rich metapelites is garnet + sillimanite + quartz + biotite + cordierite + plagioclase ± K-feldspar, whereas the most Mg-rich metapelites have orthopyroxene + garnet + biotite + quartz + cordierite + plagioclase ± K-feldspar. As these rocks occur intimately associated in the field, the variations in the mineral assemblage are controlled by the bulk composition of the rocks rather than by P–T conditions.

Five main assemblages (Table 2), ranging from Fe-rich to Mg-rich compositions, have been distinguished: orthopyroxene-free quartz-bearing metapelites (type A, Table 2); orthopyroxene-free corundum-bearing metapelites (type B, Table 2); secondary orthopyroxene-bearing metapelites (type C, Table 2); gedrite-bearing granulites (type D, Table 2); sillimanite-free orthopyroxene-bearing metapelites (type E, Table 2). Migmatitic gneisses without sillimanite and orthopyroxene with flat HREE patterns are similar in composition to orthopyroxene-free quartz-bearing metapelites. The leucosome-free metapelites have compositions typical of residual rocks: for instance, the secondary orthopyroxene-bearing rocks show high contents of FeO, MgO and Al_2O_3 and low contents of SiO_2, K_2O and Na_2O, leading to high normative corundum (up to 12 wt%). These rocks are enriched in light REE (LREE) and display negative Eu anomalies ($Eu/Eu^* = 0.50$, Fig. 2).

The orthopyroxene-free quartz-bearing metapelites (type A)

The orthopyroxene-free quartz-bearing metapelites display medium to coarse granoblastic texture with a layered structure. They consist mainly of garnet, biotite, cordierite, sillimanite, quartz and K-feldspar porphyroblasts, with subordinate plagioclase, spinel, ilmenite and graphite. Rutile, zircon and apatite are accessory phases. All the primary minerals (garnet, sillimanite, biotite and quartz) are deformed. A large variability in proportions exists from leucocratic varieties rich in quartz and K-feldspar to melanocratic varieties rich in garnet, biotite and sillimanite where quartz and K-feldspar are absent. The modal percentage of garnet varies between 2 and 25 vol%. The core of the garnet porphyroblasts frequently contains inclusions of biotite, sillimanite, quartz and plagioclase. This feature suggests the prograde reaction

$$\mathrm{Bt} + \mathrm{Sil} + \mathrm{Qtz} \pm \mathrm{Pl} \rightarrow \mathrm{Grt} + \mathrm{Melt} \pm \mathrm{Crd} \pm \mathrm{Kfs} \pm \mathrm{Ilm}. \quad (1)$$

In all samples, biotite and sillimanite are never in contact, because there are always separated by

symplectites, as a result of later reactions between them. In the presence of quartz, we observe the growth of cordierite with sometimes K-feldspar from the assemblage biotite + sillimanite + quartz, where sillimanite occurs both as porphyroblasts and as fine needles included in cordierite cores. In the absence of quartz, symplectites of cordierite + spinel and K-feldspar developed on the interfaces between primary biotite and sillimanite. This corresponds to the reactions

$$\mathrm{Bt} + \mathrm{Sil} + \mathrm{Qtz} \rightarrow \mathrm{Crd} \pm \mathrm{Kfs} + \mathrm{Melt} \quad (2)$$

and

$$\mathrm{Bt} + \mathrm{Sil} \rightarrow \mathrm{Crd} + \mathrm{Spl} \pm \mathrm{Kfs} + \mathrm{Melt}. \quad (3)$$

In a similar way, garnet porphyroblasts, in the presence of sillimanite and quartz, have been partly resorbed, being surrounded by cordierite; in quartz-free microdomains containing garnet and sillimanite, we observe the growth of cordierite toward garnet and of cordierite + spinel symplectites around sillimanite grains. These textures suggest the reactions

$$\mathrm{Grt} + \mathrm{Sil} + \mathrm{Qtz} \rightarrow \mathrm{Crd} \quad (4)$$

and

$$\mathrm{Grt} + \mathrm{Sil} \rightarrow \mathrm{Crd} + \mathrm{Spl}. \quad (5)$$

Garnet is also occasionally observed in another mineral assemblage where it occurs as euhedral grains with cordierite as result of the reaction (4), which becomes

$$\mathrm{Grt}_1 + \mathrm{Sil} + \mathrm{Qtz} \rightarrow \mathrm{Crd} + \mathrm{Grt}_2. \quad (4').$$

In some samples, a late sillimanite replaced primary sillimanite, crosscutting the foliation defined by the other phases composing the rock.

Orthopyroxene-free corundum-bearing metapelites (type B)

Corundum-bearing (quartz-free) metapelites are also the rocks richest in garnet and sillimanite. They form centimetre-sized layers. Sillimanite associated with spinel and biotite is rich in inclusions of garnet and corundum representing relics of the earlier paragenesis (Fig. 3b). This textural relationship suggests the existence of a very early melt and the corundum-consuming prograde reaction

$$\mathrm{Grt} + \mathrm{Cor} + \mathrm{Melt} + \mathrm{Ksp} \rightarrow \mathrm{Sill} + \mathrm{Spl} + \mathrm{Bt}. \quad (6)$$

The sillimanite is separated from garnet and biotite by cordierite + spinel + K-feldspar symplectites. This texture may be explained by the KFMASH univariant reaction (Fig. 3a)

$$\mathrm{Grt} + \mathrm{Bt} + \mathrm{Sil} \rightarrow \mathrm{Spl} + \mathrm{Crd} \pm \mathrm{Ksp} + \mathrm{Melt}. \quad (7)$$

These symplectites also occur on contacts of garnet or biotite with sillimanite corresponding to multivariant KFMASH equilibria (3) and (6).

Secondary orthopyroxene-bearing metapelites (type C)

Metapelites with secondary orthopyroxene are melanocratic, aluminous and consist of alternating quartz-rich and silica-undersatured sillimanite-rich layers. They are coarse-grained heterogeneous rocks with granoblastic texture and are mainly composed of sillimanite, cordierite, garnet, biotite, spinel, orthopyroxene, quartz, plagioclase and smaller amounts of ilmenite, rutile, graphite and pyrite. They are characterized by largest abundance of plagioclase with respect to K-feldspar and by spectacular crystals of sillimanite up to 10 cm in length. The garnet porphyroblasts have the same inclusions (biotite, sillimanite quartz and plagioclase) as those of the orthopyroxene-free quartz-bearing metapelites and reaction (1) should have also operated.

The breakdown of biotite in the presence of garnet with sillimanite or quartz produced symplectites of spinel + cordierite and cordierite + orthopyroxene, respectively. These textures may be explained by the reactions

$$\mathrm{Grt} + \mathrm{Bt} + \mathrm{Sil} \rightarrow \mathrm{Spl} + \mathrm{Crd} + \mathrm{Ksp} + \mathrm{Melt} \quad (7)$$

(Fig. 3c) and

$$\mathrm{Grt} + \mathrm{Bt} + \mathrm{Qtz} \rightarrow \mathrm{Crd} + \mathrm{Opx} + \mathrm{Ksp} + \mathrm{Melt}. \quad (8)$$

One sample (Tj57b) displays the breakdown of garnet to orthopyroxene, cordierite, spinel and plagioclase according to the reaction (Fig. 3d)

$$\mathrm{Grt} \rightarrow \mathrm{Opx} + \mathrm{Spl} + \mathrm{Crd} + \mathrm{Pl}(\mathrm{An}_{96}). \quad (9)$$

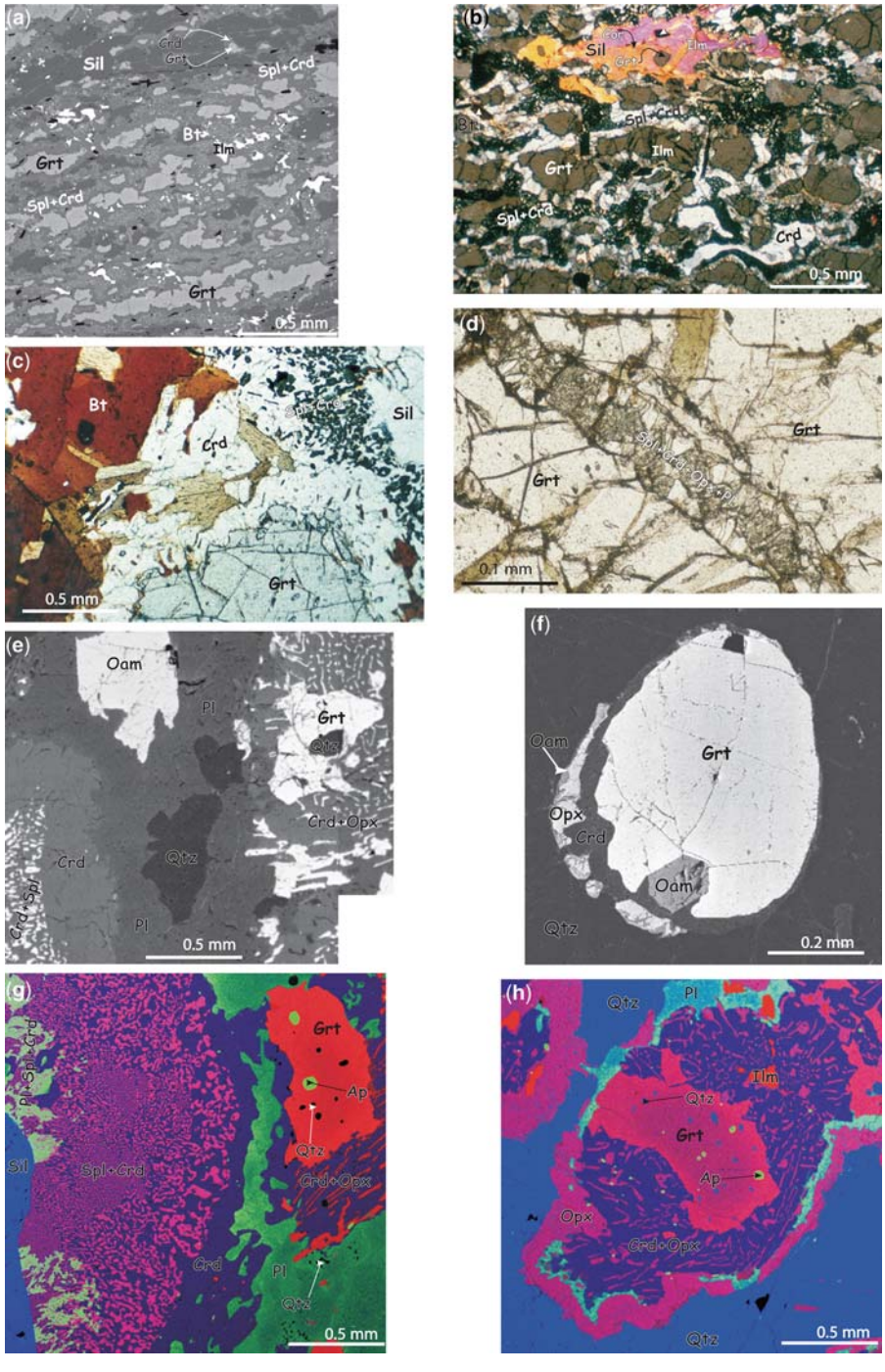

Fig. 3. Representative reaction textures of orthopyroxene-free metapelites (**a**–**d**) and orthopyroxene-bearing metapelites (**e**–**h**). (a) Primary, elongated garnet, sillimanite and biotite reacting out to cordierite–spinel in orthopyroxene-free, corundum-bearing metapelites (backscattered electron (BSE) image). (b) The same rock with sillimanite enclosing garnet, corundum and ilmenite (plane-polarized light). (c) Well-developed spinel–cordierite symplectite close to sillimanite and cordierite corona between garnet and biotite, suggesting prograde reaction

In the same sample, garnet reacted with quartz and sometimes with rutile inclusions to produce orthopyroxene and cordierite symplectites associated with ilmenite:

$$\text{Grt} + \text{Qtz} \pm \text{Rut} \rightarrow \text{Opx} + \text{Crd} \pm \text{Ilm} \pm \text{Pl}. \quad (10)$$

In the absence of biotite, garnet and sillimanite reacted to produce cordierite, spinel and quartz symplectites following the univariant FMASH reaction

$$\text{Grt} + \text{Sil} \pm \text{Melt} \rightarrow \text{Crd} + \text{Spl} + \text{Qtz} \pm \text{Ksp}. \quad (11)$$

In some microdomains, a corona of later cordierite separates spinel from quartz, suggesting the reaction

$$\text{Spl} + \text{Qtz} \rightarrow \text{Crd}. \quad (12)$$

Gedrite-bearing granulites (type D)

The gedrite-bearing rocks contain a quartz + garnet + sillimanite + cordierite + orthopyroxene + plagioclase + spinel + gedrite + ilmenite + rutile assemblage with very minor K-feldspar and biotite. They display heterogranular coarse-grained texture with spectacular coronitic and symplectitic associations. Porphyroblasts of garnet, sillimanite, quartz, gedrite, rutile and ilmenite are systematically separated by fine symplectites of orthopyroxene + cordierite ± plagioclase ± orthoamphibole or of cordierite + spinel. The orthopyroxene occurs also as coronas entirely surrounding quartz or ilmenite. Plagioclase associated with quartz is antiperthitic. Quartz occurs as discontinuous ribbons that form lenses with asymmetric tails. The texture suggests two successive reactions: sillimanite, gedrite and quartz are separated by cordierite, plagioclase and garnet corona structures (Fig. 3e); sillimanite reacted with gedrite giving cordierite–spinel symplectites associated with plagioclase or melt. These features should correspond to the reactions

$$\text{Sil} + \text{Ged} + \text{Qtz} = \text{Grt} + \text{Crd} + \text{Melt} \quad (13)$$

and

$$\text{Sil} + \text{Ged} = \text{Crd} + \text{Spl} + \text{Melt}. \quad (14)$$

Other reaction textures in these rocks are similar to those of the orthopyroxene-bearing metapelites. Garnet, quartz and sillimanite are never observed in contact and are always separated either by symplectitic or coronitic textures corresponding to reactions (4) and (5) with the implication of plagioclase (Fig. 3g). At the contact between garnet and quartz, quartz is rimmed by a corona of orthopyroxene, whereas garnet is mantled by a cordierite + orthopyroxene symplectite (Fig. 3g and h):

$$\text{Grt} + \text{Qtz} = \text{Opx} + \text{Crd} \pm \text{Pl}_2. \quad (10)$$

Locally, the orthopyroxene–cordierite symplectites are accompanied by secondary orthoamphibole and this reaction becomes (Fig. 3f)

$$\text{Grt} + \text{Qtz} \pm \text{Pl}_1 = \text{Opx} + \text{Crd} + \text{Oam} \pm \text{Pl}_2. \quad (15)$$

Opx-bearing sillimanite-free metapelites (type E)

Orthopyroxene-bearing, sillimanite-free metapelites are distinctly marked by the absence of sillimanite and the presence of orthopyroxene as primary phase. They show quartz–plagioclase–K-feldspar microdomains corresponding to leucosome. These rocks are coarse-grained with a polygonal granoblastic texture associated with a undulose extinction of quartz and kink-bands of biotite. This suggests deformation at a high temperature, contemporaneous with the granulite-facies metamorphism. The

Fig. 3. (*Continued*) Grt + Sil + Bt → Crd + Spl + Ksp (plane-polarized light). (d) Development of complex Opx + Spl + Crd + Pl intergrowths in cracks of garnet (plane-polarized light). (e) Gedrite originally in contact with primary quartz (included in garnet) and sillimanite, now enclosed by multiple coronae of phase products: plagioclase and quartz after melt, cordierite + spinel replacing sillimanite, and orthopyroxene + cordierite symplectite close to garnet (BSE image). This complex textural relationships suggests the following successive reactions: (1) Ged + Sil + Qtz → Grt + Crd + Melt; (2) Ged + Sil → Spl + Crd + Melt; (3) Grt + Qtz → Opx + Crd. (f) Close-up view of garnet and quartz breakdown to cordierite + orthopyroxene + orthoamphibole (BSE image). (g) Fine intergrowth of cordierite + spinel + calcic plagioclase close to sillimanite suggesting the reaction Grt + Sil → Crd + Spl + Pl_2, and breakdown of garnet at quartz contact giving orthopyroxene + cordierite. Layers of plagioclase and drops of quartz could represent melt phases (RGB image: red, Fe; green, Ca; blue, Al). (h) Garnet reacting out with quartz to orthopyroxene + cordierite + plagioclase (it should be noted zoning in garnet (RGB image: red, Fe; green, Ca; blue, Si).

observed minerals are orthopyroxene–garnet–biotite–plagioclase–K-feldspar–cordierite–spinel–quartz–ilmenite–rutile–zircon and apatite.

Primary orthopyroxene occurs commonly as subhedral porphyroclasts up to 1 cm in size coexisting with biotite and garnet. The presence of inclusions of biotite, quartz and garnet in the orthopyroxene suggests the prograde reaction

$$\text{Bt} + \text{Qtz} \pm \text{Grt} \rightarrow \text{Opx} + \text{Kfs} + \text{Melt}. \quad (16)$$

The spinel is also primary and occurs both as inclusions in garnet and in textural equilibrium with the association garnet–orthopyroxene–quartz–biotite–ilmenite (Fig. 4a).

The orthopyroxene porphyroclasts have exsolved garnet and small amounts of plagioclase and ilmenite lamellae mainly along (100) and (010) crystallographic planes (Fig. 4c). This feature corresponds to the reaction

$$\text{High-Al Opx} \rightarrow \text{Low-Al Opx} + \text{Grt}(+\text{Pl}+\text{Ilm}). \quad (17)$$

This reaction is generally interpreted as being indicative of isobaric cooling (Harley 1989). Locally, orthopyroxene is destabilized in Opx–Crd symplectites according to the reaction

$$\text{High-Al Opx} \rightarrow \text{Low-Al Opx} + \text{Crd}. \quad (18)$$

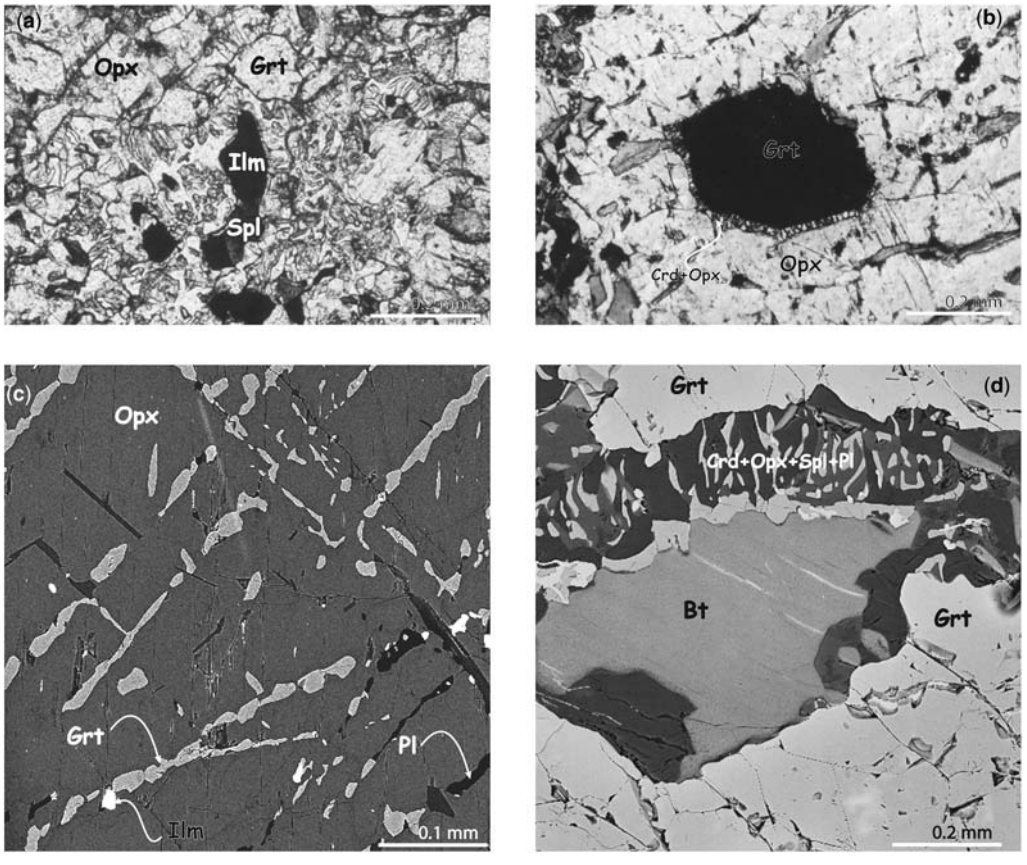

Fig. 4. Representative reaction textures of sillimanite free-metapelites. (**a**) Photomicrograph showing two successive parageneses (plane-polarized light). The primary assemblage is composed of spinel in equilibrium with quartz, garnet, biotite and orthopyroxene surrounded by secondary symplectites of cordierite + orthopyroxene$_2$ + spinel$_2$. (**b**) Late reaction observed between an inclusion of garnet and primary orthopyroxene giving very fine orthopyroxene + cordierite symplectites. (**c**) Close-up view of exsolved garnet in orthopyroxene showing two preferential directions. The presence of plagioclase and ilmenite as exsolutions in primary orthopyroxene should noted (BSE image). (**d**) Biotite and garnet breakdown to complex intergrowths of spinel + orthopyroxene + cordierite + plagioclase and secondary biotite (BSE image).

Symplectites of cordierite–orthopyroxene–spinel–plagioclase and minor biotite, ilmenite, and magnetite occur between garnet and biotite, suggesting the reaction (Fig. 4d)

$$\mathrm{Grt} + \mathrm{Bt}_1 \rightarrow \mathrm{Crd} + \mathrm{Opx} + \mathrm{Spl} + \mathrm{Pl} + \mathrm{Mt} + \mathrm{Ilm} + \mathrm{Bt}_2. \quad (19)$$

The later reactions are marked by very fine-grained symplectites of orthopyroxene and cordierite surrounding garnet and primary orthopyroxene (Fig. 4b):

$$\mathrm{Grt} + \mathrm{Opx}_1 \rightarrow \mathrm{Opx}_2 + \mathrm{Crd}. \quad (20)$$

Mineral chemistry

Representative analyses are listed in Table 3. The analyses have been performed with a CAMEBAX microprobe at the CAMPARIS centre (CNRS, Paris). The operating conditions were 15 kV accelerating voltage and 10 nA sample current. Natural silicates and synthetic oxides were used as standards for all elements, except for fluorine, which has been calibrated on fluorite. Some volumetric proportions of various phases have been determined (e.g. orthopyroxene and exsolved phases). To reconstruct the original composition of orthopyroxene before exsolution, we adopted the following procedure: (1) processing of the images made by the X-ray maps (22 500 mm^2) generated by the scanning electron microscope; (2) conversion of the obtained volumetric proportions in molar proportions by weighting molar volumes (data from Holland & Powell 1990); (3) using the phase compositions measured by the microprobe, calculation of the cation proportions and of the oxide weight per cent. For the microprobe scanning, during each analysis, the electron beam scanned a surface of 180 μm^2 (12 $\mu m \times 15$ μm); 250 analyses were carried out on adjacent areas and averaged. During calibration, standards were analysed with the same beam conditions (scanning of a 180 μm^2 area).

Garnet, in orthopyroxene-free quartz-bearing metapelites (type A, Table 3), is an almandine (64–82 mol%) rich in pyrope (12–30%) and poor in grossular and spessartine (both at 3–4 mol%). In the cores, the X_{Fe} value ranges from 0.68 in the melanosome to 0.78 in the rare grains present in the leucosome; there is a progressive increase of X_{Fe} towards the rims (to 0.86). Small euhedral garnet grains within cordierite are unzoned and have the same composition as the coarse-grained garnet rims.

In orthopyroxene-free corundum-bearing metapelites (type B, Table 3), garnet porphyroblasts have an X_{Fe} between 0.71 (core, $Alm_{67}Py_{27}Gr_2Sps_4$) and 0.84 (rim, $Alm_{76}Py_{15}Gr_2Sps_7$), whereas garnet inclusions in sillimanite have an X_{Fe} of 0.75 ($Alm_{70}Py_{23}Grs_2Sps_5$).

In secondary-orthopyroxene-bearing metapelites and gedrite-bearing granulites (types C and D, Table 3), garnet is an almandine–pyrope solid solution and shows significant X_{Fe} zoning with Fe-rich rims (Fig. 5). The largest core–rim difference (from 0.49 to 0.72) is observed in the garnet found in quartz-rich microdomains; in spinel-bearing domains, X_{Fe} ranges only from 0.60 to 0.72. Grossular and spessartine contents are always < 3 mol%. In sillimanite-free orthopyroxene-bearing metapelites, the garnet from the matrix and that included in the orthopyroxene show an increase in X_{Fe} from 0.57 to 0.73 from core ($Alm_{51}Py_{39}Gros_7Sps_4$) to rim ($Alm_{58}Py_{28}Gros_7Sps_6$). Garnet exsolved in orthopyroxene has a homogeneous composition ($Alm_{53}Py_{37}Gros_7Sps_5$) with a X_{Fe} of 0.59.

Biotite compositions are highly variable (Table 3). In orthopyroxene-free quartz-bearing metapelites (type A, Table 3), biotite inclusions in garnet have X_{Fe} in the range 0.39–0.55, with TiO_2 contents between 1 and 5.72 wt% and F content < 0.2%; biotite in the matrix is richer in Fe and Ti ($X_{Fe} = 0.50$–0.65 and $TiO_2 = 3.65$–7.47 wt%) and smaller biotite grains from the symplectites have lower contents of Fe and Ti. In orthopyroxene-free corundum-bearing metapelites (type B, Table 3), biotite has an X_{Fe} of 0.60–0.63 and contains generally up to 5 wt% TiO_2. In the secondary orthopyroxene-bearing metapelites (type C, Table 3), biotite has X_{Fe} in the range of 0.27–0.56, TiO_2 contents between 1.27 and 6.15 wt% and F in the range 0.21–0.31 wt%; larger biotite grains in the matrix are consistently richer in Fe, Ti and F. In the sillimanite-free orthopyroxene-bearing metapelites (type E, Table 3), biotite is poorer in Fe (X_{Fe} around 0.33 in contact with orthopyroxene and around 0.26 in contact with garnet) with TiO_2 and F contents around 4 wt% and 1 wt%, respectively. Three types of substitution have taken place in all assemblages: a substitution of Tschermakitic type, $Si_{-1}(Mg,Fe)_{-1}Al^{iv}_{+1}Al^{vi}_{+1}$, a substitution of titano-tschermakitic type in reverse $Ti_{-1}Al^{iv}_{-1}Mg_{+1}Si_{+2}$ and a subtitution $Ti_{-1}V_{-1}(Fe,Mn,Mg)_{+2}$ (where V is an = octahedral vacancy).

Cordierite shows a varying X_{Fe} that depends on the lithologies: 0.39–0.51 (orthopyroxene-free quartz-bearing metapelites, type A, Table 3), 0.41–0.43 (corundum-bearing metapelites, type B, Table 3), 0.22–0.39 (secondary orthopyroxene-bearing metapelites and gedrite-bearing granulites, types C and D, Table 3) and 0.19–0.26 (sillimanite-free orthopyroxene-bearing metapelites, type E, Table 3).

Table 3. *Chemical compositions of garnet, biotite, cordierite, orthopyroxene, orthoamphibole, spinel and plagioclase of metapelites from Tidjenouine area*

	Biotite											
Rock type:	Type E				Type C			Type A			Type B	
Sample:	TD 38	TD 38	TD 38	Tj 57b	Tj 59	Tj 59	TD 63	TD 39	TD 159	Tj 130	Tj 56	Tj 56
Analysis:	49	23	53	23	61	55	50	109	1	17	86	60
Position:	i/opx			c	c	s	s	c	i/grt	c	c	s
SiO_2	37.44	38.32	36.26	39.42	34.5	35.59	35.04	33.4	37.23	34.68	32.8	34.67
TiO_2	3.55	3.47	3.84	1.59	6.15	3.61	4.19	7.47	0.97	5.7	4.7	3.56
Al_2O_3	15.5	15.18	15.31	16.65	16.17	15.02	17.28	16.08	17.03	17.37	16.9	16.55
Cr_2O_3	0.64	0.72	0.79	0.05	0.18	0.04	0.25	0.06	0.05	0.19	0.05	0.29
FeO_t	11.2	10.81	13.79	12.77	19.39	21.08	20.79	22.35	16.11	22.02	21.18	19.91
MnO	0.15	0.12	0.00	0.01	0.16	0.00	0.06	0.12	0.07	0.17	0.03	0.03
MgO	16.07	17.03	14.47	18	8.72	11.49	8.25	6.57	14.12	7.42	7.94	9.27
CaO	0.03	0.00	0.00	0.02	0.00	0.16	0.06	0.00	0.00	0.00	0.08	0.04
Na_2O	0.51	0.5	0.46	0.51	0.24	0.1	0.2	0.1	0.22	0.2	0.28	0.32
K_2O	7.79	8.26	8.34	6.41	8.19	7.45	9.39	9.52	9.44	9.09	8.51	8.98
F	0.62	1.09	0.55	1.86	0.21	0.43	0.31	0.00	0.00	0.07	0.15	0.4
Cl	0.00	0.02	0.02	0.07	0.14	0.1	0.35	0.18	0.00	0.31	0.29	0.25
Sum	93.5	95.52	93.83	97.36	94.05	95.07	96.17	95.85	95.24	97.22	93.18	94.54
Si	5.554	5.562	5.462	5.565	5.334	5.447	5.354	5.195	5.576	5.267	5.208	5.378
Al^{IV}	2.446	2.438	2.538	2.435	2.666	2.553	2.646	2.805	2.424	2.733	2.792	2.622
Al^{VI}	0.264	0.159	0.18	0.335	0.28	0.156	0.465	0.143	0.582	0.377	0.371	0.404
Ti	0.396	0.379	0.435	0.169	0.715	0.415	0.481	0.874	0.109	0.651	0.561	0.415
Cr	0.075	0.083	0.094	0.006	0.022	0.005	0.03	0.007	0.006	0.023	0.006	0.036
Mg	3.553	3.684	3.249	3.787	2.009	2.621	1.879	1.523	3.152	1.68	1.879	2.143
Fe^{2+}	1.389	1.312	1.737	1.508	2.507	2.698	2.656	2.907	2.018	2.797	2.813	2.583
Mn	0.019	0.015	0.000	0.001	0.021	0.000	0.008	0.016	0.009	0.022	0.004	0.004
Ca	0.005	0.000	0.000	0.003	0.000	0.026	0.01	0.000	0.000	0.000	0.014	0.007
Na	0.147	0.141	0.134	0.14	0.072	0.03	0.059	0.03	0.064	0.059	0.086	0.096
K	1.474	1.529	1.603	1.154	1.615	1.454	1.83	1.889	1.803	1.761	1.724	1.777
F	0.291	0.5	0.262	0.83	0.103	0.208	0.15	0.000	0.000	0.034	0.075	0.196
Cl	0.000	0.005	0.005	0.017	0.037	0.026	0.091	0.047	0.000	0.08	0.078	0.066
S	15.322	15.302	15.432	15.102	15.241	15.406	15.419	15.389	15.743	15.369	15.458	15.465
X_{Fe}	0.28	0.26	0.35	0.28	0.56	0.51	0.59	0.66	0.39	0.62	0.6	0.55

(*Continued*)

Table 3. *Continued*

	Cordierite											
Rock type:	Type E		Type C			Type D		Type A		Type B		
Sample:	TD 38	TD 38	Tj 57	Tj 57b	Tj 57b	TD 67C	TD 67C	TD 39	TD 39	Tj 56	Tj 56	Tj 130
Analysis:	16	47	8	32	35	3	5	99	102	51	72	13
Position:	/bi	/opx	/opx	/opx	/sp	/spl	/opx			/sill	/grt	
SiO_2	49.94	49.95	48.73	49.97	49.22	49.79	49.29	48.41	47.86	48	48.27	49.11
TiO_2	0.00	0.06	0.00	0.03	0.02	0.01	0.05	0.00	0.00	0.12	0.03	0.01
Al_2O_3	32.66	32.34	32.31	34.12	33.78	34.37	33.5	33.07	33.02	33.52	33.39	33.19
MgO	9.75	10.94	8.6	10.78	9.62	10.1	9.02	7.57	6.38	7.21	6.88	7.63
FeO_t	5.67	4.77	7.96	5.39	6.7	6.13	7.92	10.39	11.77	10.52	10.96	9.31
MnO	0.12	0.18	0.22	0.00	0.04	0.05	0.08	0.04	0.13	0.19	0.18	0.18
CaO	0.04	0.01	0.04	0.04	0.05	0.05	0.00	0.03	0.07	0.04	0.03	0.06
Na_2O	0.18	0.19	0.2	0.12	0.12	0.14	0.13	0.08	0.09	0.13	0.12	0.08
K_2O	0.01	0.08	0.00	0.02	0.01	0.04	0.01	0.00	0.02	0.00	0.00	0.00
F	0.00	0.05	0.00	0.08	0.09	0.00	0.00	0.00	0.00	0.09	0.07	0.00
Cl	0.01	0.02	0.00	0.00	0.01	0.00	0.01	0.00	0.00	0.00	0.03	0.03
Sum	98.38	98.59	98.06	100.55	99.66	100.68	100.01	99.59	99.34	99.82	99.96	99.6
Si	5.072	5.055	5.027	4.967	4.967	4.951	4.98	4.966	4.958	4.925	4.956	5.012
Ti	0.000	0.004	0.000	0.002	0.001	0.001	0.004	0.000	0.000	0.009	0.002	0.001
Al_t	3.91	3.858	3.928	3.998	4.018	4.029	3.989	3.999	4.032	4.054	4.04	3.992
Mg	1.476	1.65	1.323	1.598	1.448	1.498	1.358	1.158	0.985	1.103	1.053	1.16
Fe^{2+}	0.482	0.404	0.686	0.448	0.566	0.51	0.67	0.891	1.02	0.903	0.941	0.794
Mn	0.01	0.015	0.02	0.000	0.003	0.004	0.007	0.003	0.011	0.016	0.016	0.016
Ca	0.004	0.001	0.004	0.004	0.005	0.005	0.000	0.003	0.008	0.004	0.004	0.007
Na	0.036	0.038	0.04	0.023	0.024	0.028	0.025	0.016	0.018	0.025	0.023	0.015
K	0.001	0.01	0.000	0.002	0.001	0.005	0.001	0.000	0.003	0.000	0.000	0.000
F	0.000	0.015	0.000	0.026	0.03	0.000	0.000	0.000	0.000	0.029	0.021	0.000
Cl	0.002	0.003	0.000	0.000	0.001	0.000	0.002	0.000	0.000	0.000	0.005	0.005
S	10.993	11.053	11.029	11.07	11.066	11.043	11.036	11.041	11.036	11.077	11.061	11.003
X_{Fe}	0.25	0.2	0.34	0.22	0.28	0.25	0.33	0.43	0.51	0.45	0.47	0.41

(*Continued*)

Table 3. *Continued*

	Garnet																
Rock type:	Type E				Type B					Type C		Type D		Type A			
Sample:	TD 38	TD 38	TD 38	TD 38	Tj 56	Tj 56	Tj 130	Tj 130	Tj 130	Tj 57	Tj 57	TD 67C	TD 67C	TD 128	TD 128	TD 63	TD 63
Analysis:	43	14	12	6	67	71	2	9	24	8	10	86	27	6	7	57	66
Position:	in opx	ex	c	r	c	r	in sill	c	r	c	r	c	r	c	r	c	r
SiO_2	39.75	38.59	39.53	37.73	36.98	37.36	37.25	37.9	37.93	35.87	36.85	39.95	37.36	36.74	38.46	38.05	36.94
TiO_2	0.07	0.00	0.02	0.03	0.08	0.00	0.04	0.08	0.00	0.12	0.07	0.00	0.06	0.03	0.00	0.03	0.00
Al_2O_3	21.67	21.41	20.99	20.62	22.12	21.75	22.18	21.3	21.35	22.17	21.37	23.02	21.69	21.68	21.76	22.03	21.94
Cr_2O_3	0.41	0.68	0.52	0.28	0.1	0.00	0.02	0.00	0.12	0.04	0.06	0.02	0.00	0.09	0.00	0.02	0.09
FeO_t	23.65	24.68	23.95	27.81	32.12	35.85	33.56	32.81	34.43	26.71	35.17	24.02	35.49	30.68	34.14	34.57	36.64
FeO	23.31	23.92	22.88	26.65	31.36	35.85	32.81	32.06	34.4	24.41	33.84	23.52	34.7	29.51	34.14	34.52	36.64
Fe_2O_3	0.38	0.85	1.19	1.29	0.84	0.00	0.84	0.84	0.03	2.55	1.48	0.56	0.88	1.30	0.00	0.06	0.00
MnO	1.73	1.96	1.81	2.87	0.66	1.8	2.02	1.67	2.63	0.29	0.82	0.29	0.98	1.15	3.00	0.92	1.51
MgO	10.16	9.87	10.07	7.14	7.09	2.97	5.84	6.3	4.19	11.02	4.88	13.18	4.93	7.36	3.32	5.14	3.00
CaO	2.54	2.4	2.74	2.42	0.83	1.00	0.53	0.53	0.59	1.11	1.52	0.85	0.88	1.20	1.02	1.08	0.89
Na_2O	0.02	0.03	0.03	0.00	0.03	0.05	0.00	0.02	0.03	0.06	0.02	0.01	0.01	0.04	0.00	0.00	0.02
K_2O	0.02	0.00	0.00	0.00	0.00	0.00	0.02	0.00	0.00	0.03	0.01	0.02	0.02	0.03	0.00	0.00	0.01
Sum	100.06	99.71	99.78	99.03	100.09	100.78	101.54	100.7	101.27	97.68	100.92	101.42	101.51	99.13	101.7	101.85	101.04
Si	3.033	2.968	3.033	2.982	2.897	2.986	2.907	2.975	3.000	2.800	2.913	2.958	2.935	2.899	3.039	2.968	2.947
Al^{IV}	0.000	0.032	0.000	0.018	0.103	0.014	0.093	0.025	0.000	0.200	0.087	0.042	0.065	0.101	0.000	0.032	0.053
Al^{VI}	1.949	1.910	1.899	1.904	1.939	2.035	1.947	1.946	1.991	1.840	1.904	1.968	1.944	1.915	2.027	1.993	2.011
Ti	0.004	0.000	0.001	0.002	0.005	0.000	0.002	0.005	0.000	0.007	0.004	0.000	0.004	0.002	0.000	0.002	0.000
Cr	0.025	0.041	0.032	0.017	0.006	0.000	0.001	0.000	0.008	0.002	0.004	0.001	0.000	0.006	0.000	0.001	0.006
Fe^{3+}	0.022	0.049	0.069	0.077	0.05	0.000	0.049	0.05	0.002	0.150	0.088	0.031	0.052	0.077	0.000	0.004	0.000
Fe^{2+}	1.487	1.539	1.468	1.762	2.054	2.396	2.141	2.104	2.275	1.594	2.237	1.457	2.28	1.947	2.256	2.252	2.445
Mg	1.155	1.131	1.152	0.841	0.828	0.354	0.679	0.737	0.494	1.282	0.575	1.454	0.577	0.865	0.391	0.597	0.357
Mn	0.112	0.128	0.118	0.192	0.044	0.122	0.134	0.111	0.176	0.019	0.055	0.018	0.065	0.077	0.201	0.061	0.102
Ca	0.208	0.198	0.225	0.205	0.07	0.086	0.044	0.045	0.05	0.093	0.129	0.067	0.074	0.101	0.086	0.09	0.076
Na	0.003	0.004	0.004	0.000	0.005	0.008	0.000	0.003	0.005	0.009	0.003	0.001	0.002	0.006	0.000	0.000	0.003
K	0.002	0.000	0.000	0.000	0.000	0.000	0.002	0.000	0.000	0.003	0.001	0.002	0.002	0.003	0.000	0.000	0.001
S	8.00	8.00	8.00	8.00	8.00	8.00	8.00	8.00	8.00	8.00	8.00	8.00	8.00	8.00	8.00	8.00	8.00
X_{Mg}	0.44	0.42	0.44	0.32	0.29	0.13	0.24	0.26	0.18	0.45	0.20	0.50	0.20	0.31	0.15	0.21	0.13
$Fe^{3+}/Fe^{3+}+Fe^{2+}$	0.01	0.03	0.04	0.04	0.02	0.00	0.02	0.02	0.00	0.09	0.04	0.02	0.02	0.04	0.00	0.00	0.00
Alm	0.5	0.51	0.5	0.59	0.69	0.81	0.71	0.7	0.76	0.53	0.75	0.49	0.76	0.65	0.77	0.75	0.82
Sps	0.04	0.04	0.04	0.06	0.01	0.04	0.04	0.04	0.06	0.01	0.02	0.01	0.02	0.03	0.07	0.02	0.03
Gr	0.07	0.07	0.08	0.07	0.02	0.03	0.01	0.01	0.02	0.03	0.04	0.02	0.02	0.03	0.03	0.03	0.03
Py	0.39	0.38	0.39	0.28	0.28	0.12	0.23	0.25	0.16	0.43	0.19	0.49	0.19	0.29	0.13	0.2	0.12

(*Continued*)

Table 3. *Continued*

	Orthopyroxene							
Rock type:	Type D		Type C		Type E			
Sample:	TD 67A	TD 67C	Tj 57b	Tj 57b	TD 38	TD 38	TD 38	TD 38
Analysis:	45	101	38	16	14	40	16	Opx I
Position:	/crdsp	/crd	/qz	/sp	Sympl splcrd	r/crd	c	reconstituted
SiO_2	49.6	49.48	51.01	50.8	51.62	51.26	50.75	48.27
TiO_2	0.16	0.06	0.06	0.1	0.22	0.08	0.1	0.37
Al_2O_3	4.64	2.96	1.46	3.4	2.49	3.4	4.85	6.24
Cr_2O_3	0.16	0.05	0.00	0.01	0.26	0.34	0.54	0.55
FeO_t	25.73	31.51	30.54	26.05	25.75	22.58	21.36	21.53
FeO	25.73	31.51	30.54	26.05	25.75	22.58	21.36	19.57
Fe_2O_3	0.00	0.00	0.00	0.00	0.00	0.00	0.00	2.18
MnO	0.3	0.33	0.22	0.16	1.13	1.26	0.6	0.95
MgO	18.41	15	16.66	19.28	17.39	20.53	21.55	20.26
CaO	0.09	0.14	0.17	0.19	0.13	0.12	0.08	0.4
Na_2O	0.01	0.05	0.00	0.00	0.01	0.03	0.03	0.05
K_2O	0.00	0.01	0.00	0.00	0.02	0.00	0.00	0.22
Sum	99.1	99.59	100.12	99.99	99.02	99.6	99.86	99.06
Si	1.896	1.935	1.971	1.922	1.995	1.928	1.887	1.819
Al^{IV}	0.104	0.065	0.029	0.078	0.005	0.072	0.113	0.181
Al^{VI}	0.105	0.071	0.038	0.073	0.108	0.079	0.099	0.096
Alt	0.209	0.136	0.067	0.152	0.113	0.151	0.213	0.277
Ti	0.005	0.002	0.002	0.003	0.006	0.002	0.003	0.01
Cr	0.005	0.002	0.000	0.000	0.008	0.01	0.016	0.016
Fe^{3+}	0.000	0.000	0.000	0.000	0.000	0.000	0.000	0.062
Fe^{2+}	0.823	1.03	0.987	0.824	0.832	0.71	0.664	0.617
Mg	1.049	0.874	0.959	1.087	1.001	1.151	1.194	1.138
Mn	0.01	0.011	0.007	0.005	0.037	0.04	0.019	0.03
Ca	0.004	0.006	0.007	0.008	0.005	0.005	0.003	0.016
Na	0.001	0.004	0.000	0.000	0.001	0.002	0.002	0.004
K	0.000	0.000	0.000	0.000	0.001	0.000	0.000	0.011
Total	4.00	4.00	4.00	4.00	4.00	4.00	4.00	4.00
X_{Mg}	0.56	0.46	0.49	0.57	0.55	0.62	0.64	0.65

(*Continued*)

Table 3. *Continued*

Rock type:	Orthoamphibole									
	Type D									
Sample:	TD 67	TD 67	TD 67	TD 67	TD 67	TD 67	TD 67	TD 67	TD 67	TD 67
Analysis:	117	47	27	100	63	12	74	21	32	21
Position:	c	c	c	c	r	r	r	s	s	s
SiO_2	42.72	40.44	40.17	38.47	49.72	44.2	43.43	50.09	45.89	45.97
TiO_2	0.62	1.27	0.51	0.16	0.06	0.9	0.78	0.07	0.56	0.69
Al_2O_3	15.91	16.1	19.34	20.45	14.81	13.5	14.39	6.58	8.43	12.15
Cr_2O_3	0.00	0.17	0.2	0.00	0.08	0.16	0.16	0.14	0.08	0.11
FeO_t	23.19	23.9	22.85	20.22	19.21	22.64	21.77	25.68	26.94	22.6
MnO	0.16	0.25	0.28	0.12	0.28	0.2	0.33	0.11	0.19	0.24
MgO	13.37	11.74	12.41	14.6	12.48	14.25	14.08	15.72	14.73	14.91
NiO	0.00	0.00	0.00	0.00	0.00	0.00	0.00	0.00	0.00	0.00
ZnO	0.22	0.00	0.00	0.04	0.01	0.02	0.19	0.00	0.00	0.00
CaO	0.69	0.69	0.6	0.31	0.17	0.53	0.53	0.09	0.49	0.6
Na_2O	1.74	2.05	2.14	2.34	0.12	1.7	1.92	0.07	0.75	1.45
K_2O	0.04	0.05	0.03	0.02	0.14	0.06	0.00	0.01	0.03	0.00
F	0.22	0.14	0.37	0.43	0.13	0.36	0.2	0.00	0.02	0.46
Cl	0.12	0.12	0.09	0.03	0.00	0.00	0.09	0.02	0.03	0.07
Sum	99.00	96.92	98.99	97.19	97.21	98.52	97.87	98.58	98.14	99.25
Si	6.275	6.123	5.918	5.718	7.098	6.499	6.415	7.326	6.874	6.693
Al^{IV}	1.725	1.877	2.082	2.282	0.902	1.501	1.585	0.674	1.126	1.307
Al^{VI}	1.03	0.996	1.276	1.3	1.59	0.838	0.92	0.46	0.362	0.778
Ti	0.069	0.145	0.057	0.018	0.006	0.1	0.087	0.008	0.063	0.076
Cr	0.000	0.02	0.023	0.000	0.009	0.019	0.019	0.016	0.009	0.013
Mg	2.928	2.65	2.726	3.235	2.656	3.124	3.1	3.427	3.289	3.236
Fe^{2+}	2.849	3.026	2.815	2.513	2.293	2.784	2.689	3.141	3.375	2.752
Mn	0.02	0.032	0.035	0.015	0.034	0.025	0.041	0.014	0.024	0.03
Ni	0.000	0.000	0.000	0.000	0.000	0.000	0.000	0.000	0.000	0.000
Zn	0.024	0.000	0.000	0.004	0.001	0.002	0.021	0.000	0.000	0.000
Ca	0.109	0.112	0.095	0.049	0.026	0.083	0.084	0.014	0.079	0.094
Na	0.496	0.602	0.611	0.674	0.033	0.485	0.55	0.02	0.218	0.409
K	0.007	0.01	0.006	0.004	0.025	0.011	0.000	0.002	0.006	0.000
F	0.102	0.067	0.172	0.202	0.059	0.167	0.093	0.000	0.009	0.212
Cl	0.03	0.031	0.022	0.008	0.000	0.000	0.023	0.005	0.008	0.017
$\sum$	15.53	15.592	15.643	15.813	14.674	15.47	15.511	15.102	15.426	15.387
X_{Mg}	0.507	0.467	0.492	0.563	0.537	0.529	0.536	0.522	0.494	0.54

Table 3. *Continued*

	Spinel											
Rock type:	Type D		Type E			Type C		Type B			Type A	
Sample:	TD 67N	TD 67C	TD 38	TD 38	TD 38	Tj 57b	Tj 57b	Tj 56	Tj 56	Tj 130	TD 128	TD 159
Analysis:	47	35	27	28	55	6	15	48	75	19	110	10
SiO_2	0.02	0.01	2.79	0.11	0.00	0.00	0.03	0.01	0.04	0.00	0.00	0.07
TiO_2	0.26	0.1	0.74	0.3	0.21	0.08	0.09	0.14	0.2	0.01	0.13	0.02
Al_2O_3	58.76	59.58	29.57	46.78	43.98	60.31	57.9	58.53	58.91	59.28	56.46	61.67
Cr_2O_3	0.93	0.16	24.86	13.42	16.13	0.08	0.15	0.00	0.06	0.17	0.00	0.00
Fe_2O_3	2.41	2.17	0.00	2.24	0.16	2.64	3.07	2.42	1.09	1.40	3.61	0.00
MgO	7.24	5.53	1.96	6.51	5.99	8.08	4.78	3.64	3.12	3.80	4.15	0.04
FeO	30.47	33.14	34.94	27.8	27.66	29.00	33.41	35.55	36.64	35.37	33.83	36.78
MnO	0.00	0.12	0.76	0.55	0.34	0.00	0.16	0.1	0.21	0.38	0.33	0.02
ZnO	n.a.	0.08	n.a.	n.a.	n.a.	0.45	0.38	0.2	0.08	0.01	n.a.	n.a.
CaO	0.02	0.00	0.35	0.21	0.00	0.03	0.00	0.00	0.01	0.00	0.00	0.00
Na_2O	0.01	0.00	0.12	0.05	0.07	0.00	0.01	0.05	0.00	0.00	0.00	0.00
K_2O	0.00	0.00	0.00	0.16	0.00	0.01	0.00	0.00	0.00	0.00	0.02	0.00
Sum	100.13	100.91	96.65	98.28	95.39	100.67	100.03	100.63	100.38	100.55	98.53	98.6
Si	0.001	0.000	0.092	0.003	0.000	0.000	0.001	0.000	0.001	0.000	0.000	0.002
Ti	0.005	0.002	0.018	0.007	0.005	0.002	0.002	0.003	0.004	0.001	0.003	0.000
Al	1.918	1.947	1.145	1.626	1.598	1.941	1.926	1.945	1.964	1.964	1.917	2.076
Cr	0.02	0.003	0.646	0.313	0.393	0.002	0.003	0.000	0.001	0.004	0.000	0.000
Fe^{3+}	0.05	0.045	0.000	0.05	0.004	0.054	0.065	0.051	0.023	0.030	0.078	0.000
Mg	0.299	0.229	0.096	0.286	0.275	0.329	0.201	0.153	0.132	0.159	0.178	0.002
Fe^{2+}	0.706	0.768	0.96	0.686	0.713	0.662	0.789	0.838	0.867	0.831	0.815	0.879
Mn	0.000	0.003	0.021	0.014	0.009	0.000	0.004	0.002	0.005	0.009	0.008	0.000
Zn		0.002				0.009	0.008	0.004	0.002	0.002		
Ca	0.001	0.000	0.012	0.007	0.000	0.001	0.000	0.000	0.000	0.000	0.000	0.000
Na	0.001	0.000	0.008	0.003	0.004	0.000	0.000	0.003	0.000	0.000	0.000	0.000
K	0.000	0.000	0.000	0.006	0.000	0.000	0.000	0.000	0.000	0.000	0.001	0.000
Sum	3.000	3.001	3.057	3.016	3.081	3.000	3.003	3.000	3.001	3.000	3.000	2.959
$X_{Fe^{2+}}$	0.7	0.77	0.91	0.71	0.72	0.67	0.8	0.85	0.87	0.839	0.82	1

(*Continued*)

Table 3. *Continued*

	Plagioclase												
Rock type:	Type A		Type B	Type C		Type D				Type E			
Sample:	TD 63	TD 63	Tj 56	Tj 57b	Tj 59	TD 67C	TD 67C	TD 67C	TD 67C	TD 38	TD 38	TD 38	TD 38
Analysis:	45	61	74	17	56	75	43	26	44	17	25	17	21
Position:			s	s			/Qtz	/Qtz	opxcrdspl	s	s	exsol	matrix
SiO_2	60.37	61.46	56.2	45.01	62.34	62.16	59.84	56.76	43.78	45.86	48.72	54.97	55.06
TiO_2	0.09	0.00	0.02	0.01	0.01	0.02	0.03	0.00	0.07	0.08	0.05	0.00	0.01
Al_2O_3	26	25.2	26.49	36.13	25.31	24.45	25.69	28.31	35.86	34.03	32.56	28.19	28.86
Cr_2O_3	0.00	0.00	0.00	0.05	0.03	0.00	0.09	0.06	0.00	0.00	0.16	0.04	0.00
Fe_2O_3	0.00	0.00	0.00	0.00	0.00	0.00	0.00	0.00	0.00	0.00	0.00	0.00	0.00
MgO	0.02	0.00	0.01	0.00	0.02	0.03	0.00	0.00	0.02	0.03	0.02	0.18	0.00
FeO	0.00	0.11	0.22	0.34	0.12	0.05	0.39	0.41	0.37	0.44	0.48	0.82	0.37
MnO	0.00	0.03	0.07	0.03	0.01	0.00	0.02	0.00	0.00	0.00	0.07	0.04	0.00
CaO	6.55	6.01	8.76	19	5.89	5.28	6.9	9.73	19.25	17.89	15.85	10.89	11.54
Na_2O	7.68	7.96	7.02	0.48	7.81	8.79	7.52	6.05	0.76	1.12	2.21	5.1	5.11
K_2O	0.21	0.37	0.04	0.00	0.23	0.34	0.11	0.12	0.02	0.05	0.02	0.06	0.04
Sum	101	101.18	98.89	101.06	101.77	101.17	100.65	101.52	100.14	99.6	100.15	100.28	101.09
Si	2.661	2.702	2.558	2.056	2.716	2.731	2.654	2.518	2.027	2.124	2.228	2.478	2.463
Ti	0.003	0.000	0.001	0.000	0.000	0.001	0.001	0.000	0.002	0.003	0.002	0.000	0.000
Al	1.351	1.306	1.421	1.946	1.299	1.266	1.343	1.48	1.957	1.858	1.755	1.498	1.522
Cr	0.000	0.000	0.000	0.002	0.001	0.000	0.003	0.002	0.000	0.000	0.006	0.001	0.000
Fe^{3+}	0.000	0.000	0.000	0.000	0.000	0.000	0.000	0.000	0.000	0.000	0.000	0.000	0.000
Mg	0.001	0.000	0.001	0.000	0.001	0.002	0.000	0.000	0.001	0.002	0.002	0.012	0.000
Fe^{2+}	0.000	0.004	0.009	0.013	0.004	0.002	0.014	0.015	0.014	0.017	0.018	0.031	0.014
Mn	0.000	0.001	0.003	0.001	0.001	0.000	0.001	0.000	0.000	0.000	0.003	0.001	0.000
Ca	0.309	0.283	0.427	0.93	0.275	0.249	0.328	0.463	0.955	0.888	0.777	0.526	0.553
Na	0.656	0.678	0.62	0.043	0.66	0.749	0.647	0.521	0.068	0.101	0.196	0.446	0.443
K	0.012	0.021	0.002	0.000	0.013	0.019	0.006	0.007	0.001	0.003	0.001	0.003	0.002
Sum	4.99	5.00	5.04	4.99	4.97	5.02	5.00	5.01	5.03	5.00	4.99	5.00	5.00
X_{an}	0.32	0.29	0.41	0.956	0.29	0.245	0.334	0.467	0.933	0.895	0.798	0.539	0.554
X_{ab}	0.67	0.69	0.59	0.044	0.7	0.736	0.66	0.526	0.067	0.102	0.201	0.457	0.444
X_{or}	0.01	0.02	0.000	0.000	0.01	0.019	0.006	0.007	0.001	0.003	0.001	0.003	0.002

c, core; r, rim; s, symplectite.

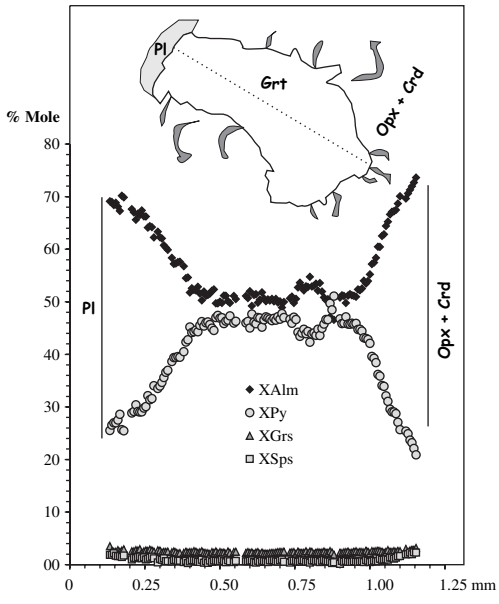

Fig. 5. Compositional profile across garnet in gedrite-bearing granulites.

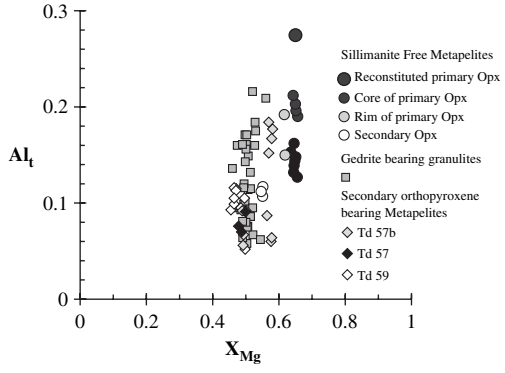

Fig. 6. Plot of X_{Mg} v. Al_t (cations p.f.u.) in orthopyroxene of the orthopyroxene-bearing + metapelites.

Orthopyroxene has the same composition in the gedrite-bearing granulites and metapelites with secondary orthopyroxene (types C and D, Table 3): X_{Fe} ranges between 0.43 and 0.58 (average of 0.50) and Al_2O_3 from 1.2 to 4.7 wt%; the most aluminous orthopyroxene is found in the symplectites (both the spinel + cordierite + orthopyroxene ± plagioclase and the cordierite + orthopyroxene symplectites) and in the orthopyroxene around quartz. In sillimanite-free orthopyroxene-bearing metapelites (type E, Table 3), the orthopyroxene in the symplectites show a X_{Fe} around 0.43 and Al_2O_3 contents between 2 and 3 wt%. Where exsolution occurs, the primary orthopyroxene is poorer in Fe (X_{Fe} 0.34–0.39) and richer in Al_2O_3 (3.65–5.8 wt%; Fig. 6). Image analysis and microprobe scanning (see analytical techniques above) have allowed us to estimate the composition of the primary orthopyroxene before exsolution: the two methods give similar results with X_{Fe} around 0.35 and Al_2O_3 contents close to 6.5 wt%.

Orthoamphibole has a formula based on 23 equivalent oxygen-when calculated according to Spear (1980); this method gives the lowest Fe^{3+} compatible with stoichiometry, which corresponds to a maximum of Na assigned to the A-site. The composition of the Tidjenouine orthoamphibole is highly variable (X_{Fe} 0.43–0.54, Al_2O_3 6.58–21.50 wt%, Na_2O 0.07–2.47 wt%, TiO_2 0.02–1.27 wt%; type D, Table 3, Fig. 7a and b) but always have enough Al to be considered on the gedrite side of the gedrite–anthophyllite solid solution. The variability in Al_2O_3 indicates, however, the absence of a miscibility gap, suggesting a temperature of crystallization above 600 °C (Spear 1980). The highest Al_2O_3 and Na_2O values are found in the core of millimetre-sized elongated zoned grains. Orthoamphibole in symplectites have similar compositions to the rims of coarse-grained gedrite. Several substitutions have taken place (Fig. 8): a substitution of edenitic type ($Si_{-1}(Na,K)^{A}_{+2}Al^{IV}_{+1}$; the slope of 0.56 in Figure 8 implies also a compensatory Tschermakitic substitution in reverse ($Al^{IV}_{-1}Al^{VI}_{-1}Mg_{+1}Si_{+1}$). These two substitutions correspond to the pargasitic type substitution (Robinson *et al.* 1971). An additional titano-Tschermakitic substitution ($Si_{+2}Mg_{+1}Ti_{-1}Al^{IV}_{-2}$) also occurred. These three substitutions imply that Al^{IV} = A-site occupancy + ($Al^{VI} + Fe^{3+} + 2Ti$) (Robinson *et al.* 1971; Czarmanske & Wones 1973); indeed, the substitution of Na in the A-Site and Ti in the octohedral site must be compensated by the substitution of Al for Si in the tetrahedral sites.

Spinel composition has a large variability related to the bulk-rock composition: Fe-rich hercynite–spinel solid solution in sillimanite-bearing metapelites (Table 3); Fe-rich ($0.82 < X_{Fe} < 1$) hercynite with nearly no chromite (<0.03%), no Zn and Fe^{3+} in orthopyroxene-free quartz-bearing metapelites (type A, Table 3) and corundum-bearing metapelites (type B; Table 3); spinel-rich hercynite (no Cr, $0.67 < X_{Fe} < 0.79$) in metapelites with secondary orthopyroxene and gedrite-bearing rocks (types C and D, Table 3); and ternary solid solution between hercynite, chromite and spinel in sillimanite-free orthopyroxene-bearing metapelites (type E, Table 3). The spinel in the symplectites with orthopyroxene–cordierite–plagioclase–ilmenite–magnetite

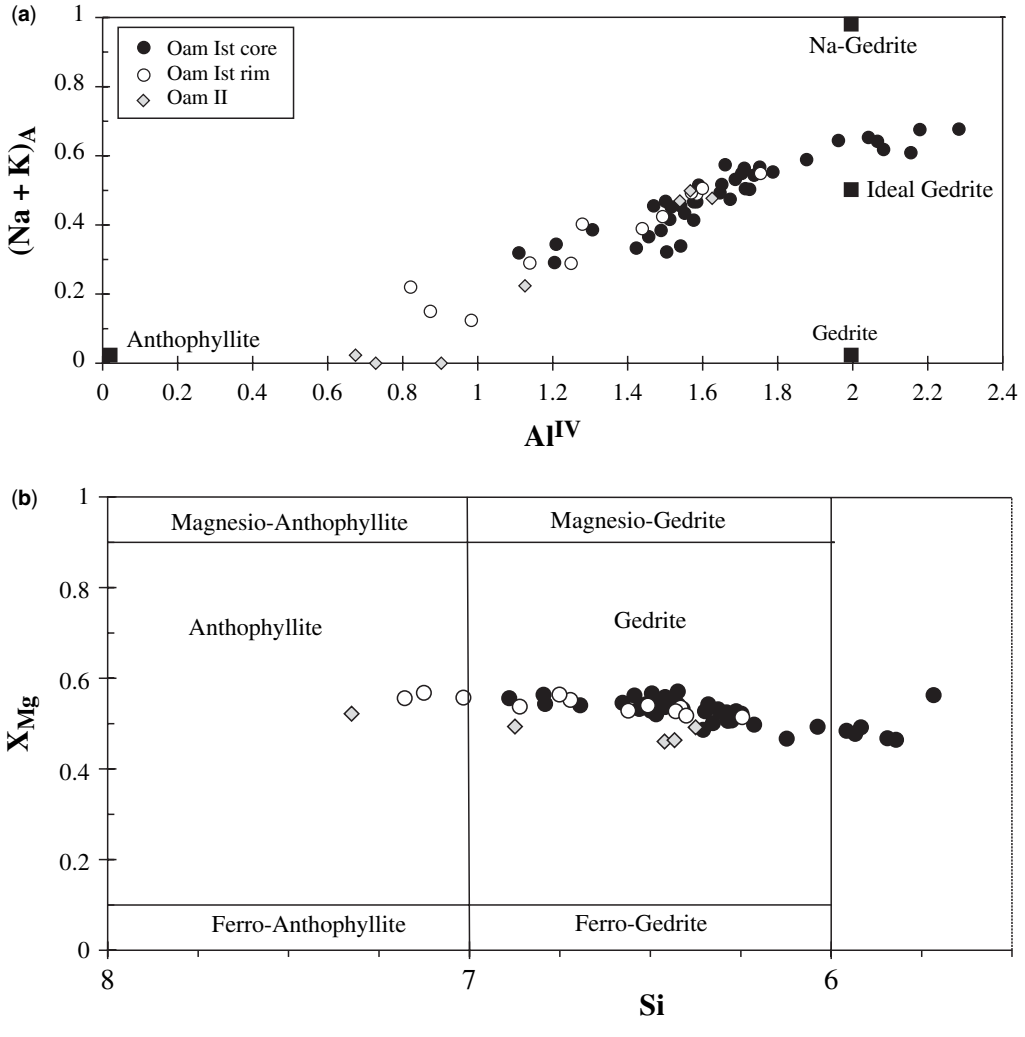

Fig. 7. Plot of orthoamphibole chemical compositions. (**a**) $(Na + K)_A$ v. Al^{IV}; (**b**) Si v. X_{Mg}, after Leake *et al.* (1997).

($Herc_{55}Chr_{39}Sp_6$, $X_{Fe} = 0.90$) is consistently richer in in Mg and Cr ($Cr_2O_3 = 25.73$ wt%) than the spinel in contact with quartz ($Herc_{60}Chr_{26}Sp_{14}$, $X_{Fe} = 0.70$); in both cases, Fe^{3+} is negligible.

Plagioclase is highly variable in composition, but each given rock type and/or microdomain has its own characteristics. Plagioclase has a rather constant composition in the orthopyroxene-free metapelites (type A, Table 3: An_{25-34}), with the richest. An composition found in the inclusions in garnet, whereas it has a highly variable composition in the gedrite-bearing granulites (type D, Table 3): An_{75-92} in the symplectites with orthopyroxene and cordierite; An_{27-47} in contact with quartz at the margin of symplectites, and An_{17-33} when included in quartz and sillimanite. Plagioclase around gedrite is zoned, showing increasing X_{An} from the contact with gedrite (An_{23}) towards the periphery (An_{47}). In the secondary-orthopyroxene-bearing metapelites (type C, Table 3), the plagioclase in the leucosome is an unzoned oligoclase (An_{30}) whereas the plagioclase in the spinel–orthopyroxene–cordierite symplectites in fissures in garnet has an almost pure anorthite composition (An_{95-97}). Plagioclase from sillimanite-free orthopyroxene-bearing metapelites (type E, Table 3) shows large X_{An} variation according to the microdomain: between 0.75 and 0.92 in symplectites; 0.50 and 0.58 in plagioclase exsolved by orthopyroxene, and $0.45 < X_{An} < 0.57$ in matrix plagioclase.

Alkali-feldspar displays 60–99 mol% of orthoclase component.

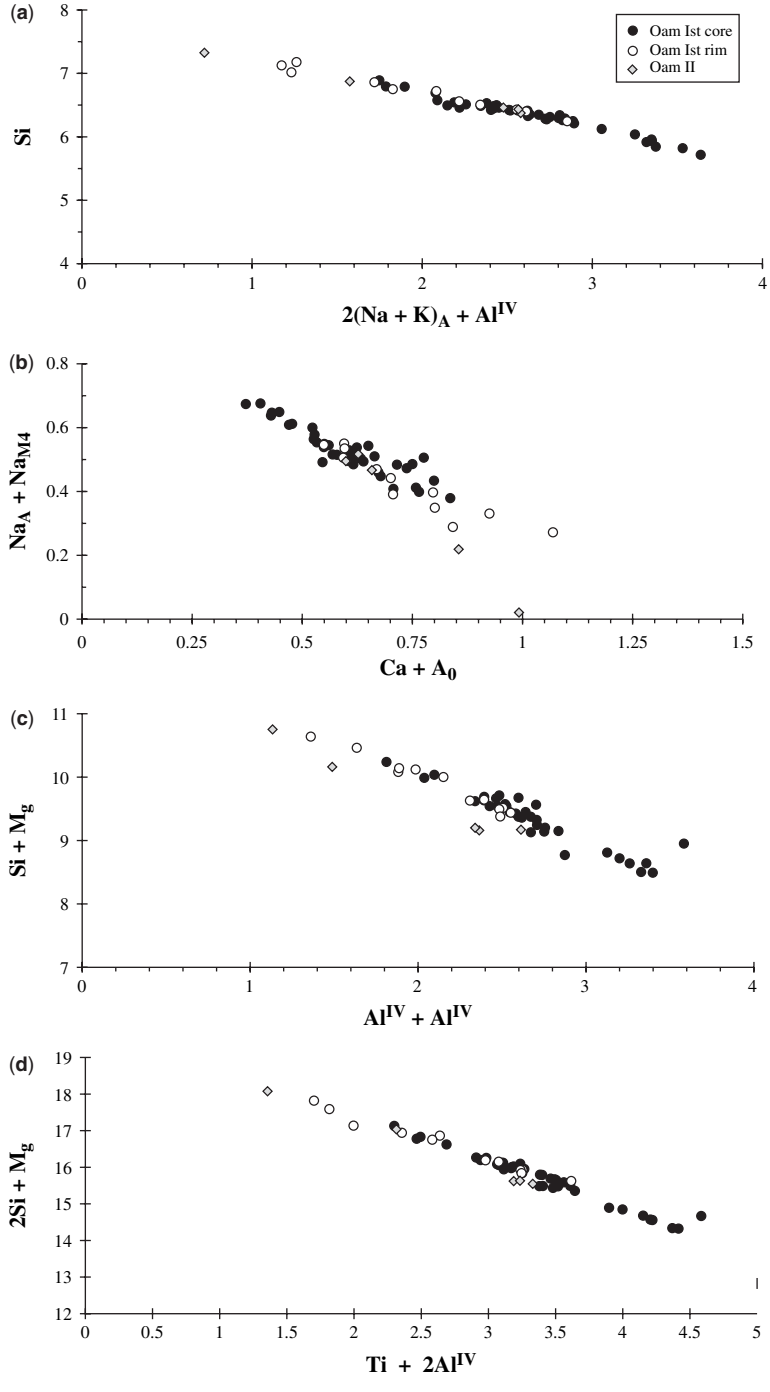

Fig. 8. Orthoamphibole substitutions in gedrite-bearing granulites.

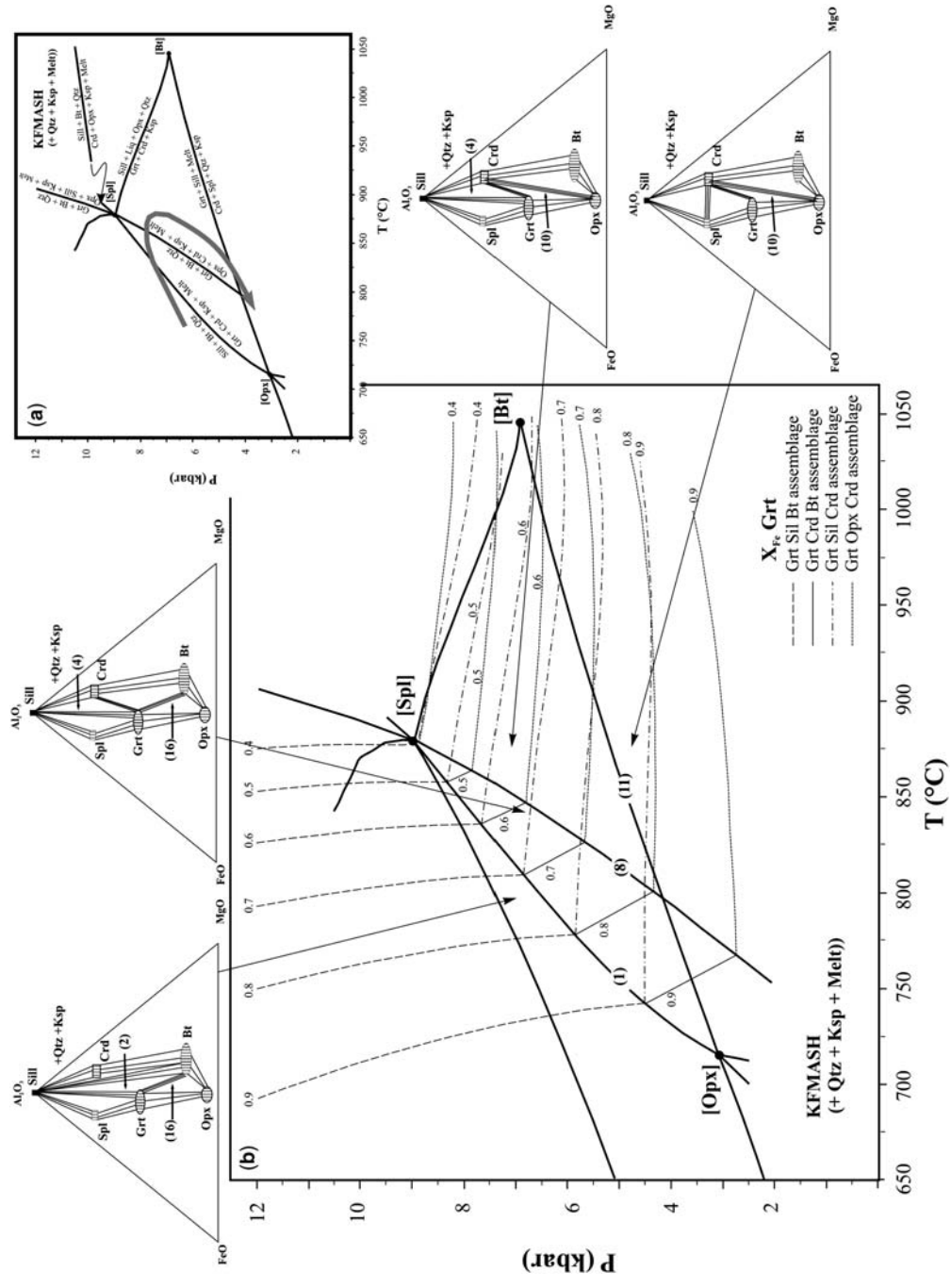
(a)
KFMASH
(+ Qtz + Ksp + Melt)
[Spl]
[Bt]
[Opx]
P (kbar)
T (°C)
(b)
[Spl]
[Bt]
[Opx]
(1)
(8)
(11)
KFMASH
(+ Qtz + Ksp + Melt)
X_{Fe} Grt
Grt Sil Bt assemblage
Grt Crd Bt assemblage
Grt Sil Crd assemblage
Grt Opx Crd assemblage
P (kbar)
T (°C)
Al2O3
Sill
+Qtz +Ksp
Crd
Spl
Grt
Bt
Opx
FeO
MgO
(2)
(4)
(16)
(10)

The other minerals are: ilmenite (Ilm_{96-100} with Mg and Mn $< 2-3$ mol%); magnetite, present only in sample TD38 as very rare coarse intergrowths with spinel–ilmenite–orthopyroxene–cordierite–plagioclase and is pure Fe_3O_4; graphite, ubiquitous in metapelites; and pyrite, abundant in secondary-orthopyroxene-bearing metapelites.

Petrological and $P-T$ evolution

Several petrogenetical grids are presented.

(1) A KFMASH petrogenetic grid involving garnet–orthopyroxene–sillimanite–biotite–melt–K-feldspar–quartz–cordierite–spinel, calculated using Thermocalc 3.1 software (Powell *et al.* 1998; Fig. 9). Compatibility diagrams were drawn interpret the textures and to work out the theoretical reactions in the KFMASH system. Representative analyses of coexisting phases have been projected from quartz and K-feldspar onto the AFM triangle (Fig. 10). These diagrams show the different stable assemblages derived from textural observations and mineral chemistry as well as the reaction sequences in the quartz-bearing metapelites. These diagrams together with the textural relationships in the Tidjenouine metapelites indicate the prograde crossing of the univariant reaction (1), Sill + Bt + Qtz → Grt + Crd + Ksp + Melt, suggested by remnants of biotite, sillimanite and quartz in garnet and cordierite (Fig. 9a). The near metamorphic peak is represented by the crossing of the univariant reaction (8), Grt + Bt + Qtz → Opx + Crd + Ksp + Melt, which is observed in all orthopyroxene-bearing metapelites. During the decompressional stage, the degenerated reaction (11), Grt + Sill → Crd + Spl + Qtz, occurs. The X_{Fe} isopleths of garnet with Qtz and Melt in excess (divariant assemblages: Grt Sil Bt, Grt Crd Bt, Grt Sil Crd and Grt Opx Crd) are also represented in Figure 9b. These isopleths are very P-dependent and constitute a good geobarometer. The core composition of the most magnesian garnet (typical X_{Fe} of 0.5), which is observed in orthopyroxene-bearing assemblages, gives a good estimate of the maximum possible pressure, which can be fixed between 7 and 8 kbar.

(2) A KFMASH petrogenetic grid involving garnet–corundum–sillimanite–biotite–cordierite–spinel–melt–K-feldpar and water (Fig. 11a). It consists of two invariant points, [H_2O] and [Cor], and the univariant reactions that emanate from them (Fig. 11b). The sequence of mineral reactions is well illustrated in Figure 11b. The corundum-consuming reaction (6), Grt + Cor + Melt + Ksp → Sill + Spl + Bt (H_2O, Crd)), should occur before the breakdown of biotite and sillimanite with primary garnet to produce a cordierite assemblage (reaction (7), Grt + Bt + Sill → Spl + Crd + Melt + Ksp) (Fig. 11a and b).

(3) An FMASH petrogenetic grid involving garnet–orthopyroxene–sillimanite–biotite–gedrite–quartz–cordierite–spinel and water is the same as that constructed by Ouzegane *et al.* (1996) for $aH_2O = 1$ (Fig. 11a). All reactions at the invariant points are dehydration reactions and therefore lowering aH_2O to 0.6 or 0.2, which is in agreement with granulite-facies conditions, should lower the temperature of the invariant points. In this grid, only reactions producing garnet are observed, and the univariant FMASH reaction (13), Oam + Sill + Qtz → Grt + Crd, is crossed during the prograde stage.

A $P-T$ pseudosection has also been constructed for quartz-bearing microdomains (with representative composition: FeO 11.5 mol%, MgO 7 mol%, Al_2O_3 16 mol%, SiO_2 65.5 mol% and $aH_2O = 1$; Fig. 11b). This pseudosection accounts qualitatively for the paragenetic evolution; thus, it shows a very complete history of the $P-T$ evolution of the gedrite-bearing granulites by successive divariant and trivariant assemblages. The occurrence of sillimanite + gedrite at an early stage of evolution, giving garnet + gedrite + sillimanite and garnet + sillimanite (M_1 peak assemblage), implies an increase of temperature before the decompression marked by the growth of cordierite + orthopyroxene symplectites (M_2). Afterwards, the assemblage orthopyroxene + cordierite + orthoamphibole (M_2') indicates a decrease of temperature in the latest stage. This demonstrates that the Tidjenouine rocks have recorded a clockwise $P-T$ evolution. All these stages (M_1, M_2 and M_2') most probably occurred during the same metamorphic event.

The evolution of pressure and temperature of the Tidjenouine granulite-facies metamorphism has been also determined using internally consistent datasets (average $P-T$ option of Thermocalc, Powell & Holland 1988) and independently calibrated geothermometers and geobarometers. The results are summarized in Table 4. The

Fig. 9. Petrogenetic grid in KFMASH system representing quartz-bearing metapelites calculated using Thermocalc (Powell & Holland 1998). (**a**) Reactions and preferred $P-T$ path; (**b**) plot of isopleths of X_{Fe} in garnet in different assemblages. Compatibility diagrams are derived from the KFMASH system after projection from quartz, water and K-feldspar (KSH) onto the AFM triangle. Reaction numbers are as in text.

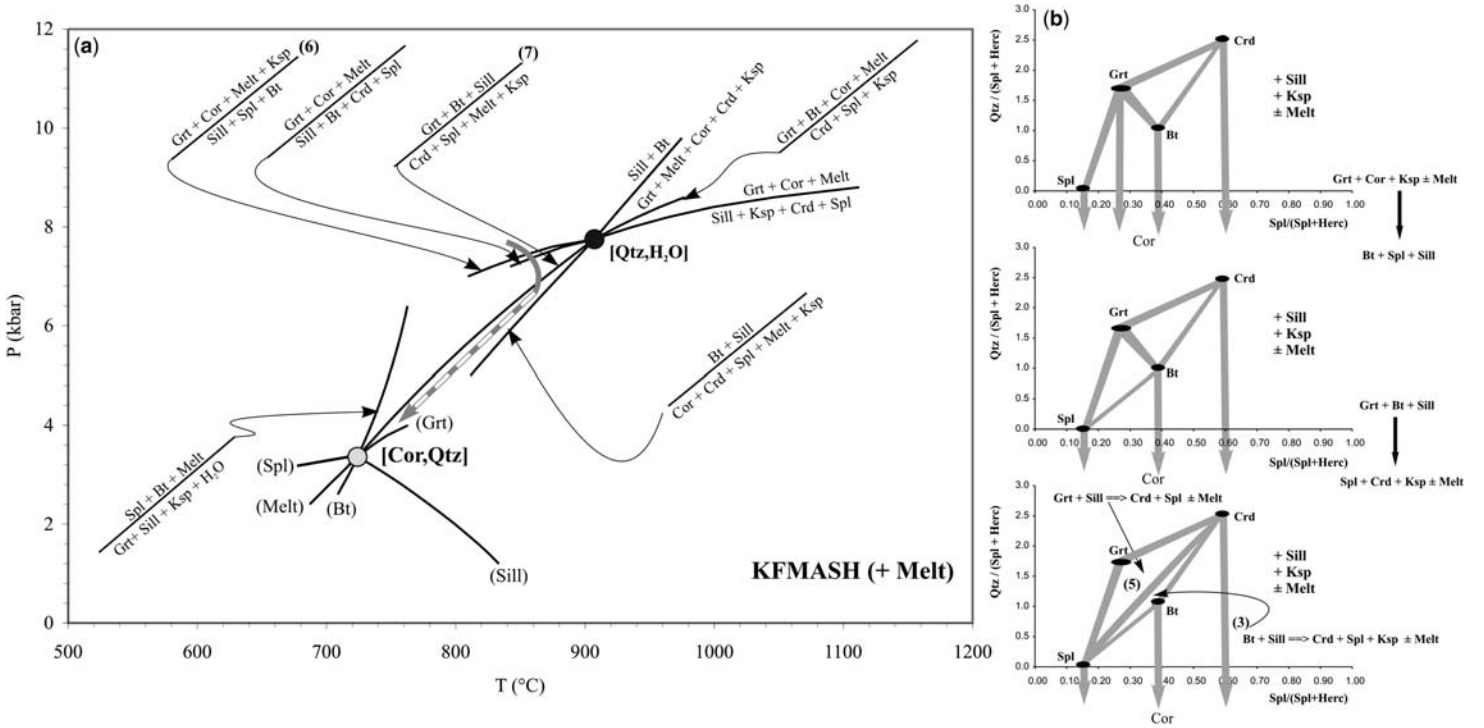

Fig. 10. Petrogenetic grid in KFMASH system representing quartz-free metapelites, calculated using Thermocalc software (Powell & Holland 1998). (**a**) Reactions and preferred P–T path; (**b**) compatibility diagrams derived from the KFMASH system after projection from sillimanite, water, K-feldspar and melt onto the quartz–spinel–hercynite plane. Reaction numbers are as in text.

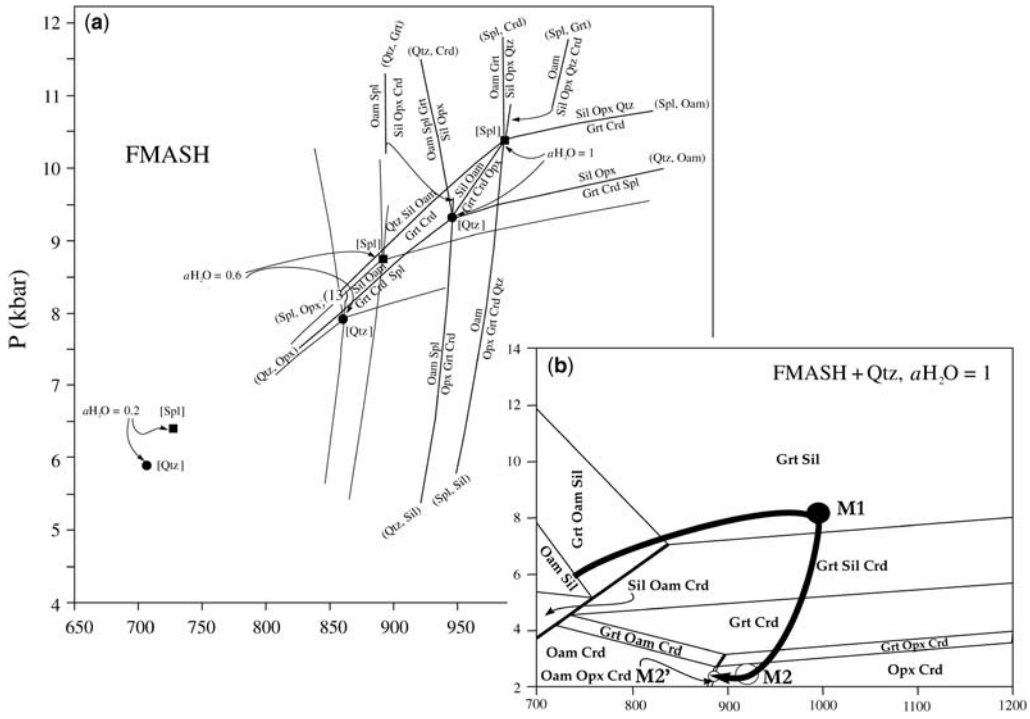

Fig. 11. Petrogenetic grid and $P-T$ pseudosection in FMASH system representing gedrite-bearing metapelites calculated using Thermocalc software (Powell & Holland 1998). (**a**) Petrogenetic grid showing the displacement of invariant points and univariant reactions depending on aH_2O. Reaction numbers are as in text. (**b**) $P-T$ pseudosection for a fixed bulk composition (mol%: FeO 11.5, MgO 7, Al_2O_3 16, SiO_2 65.5) and $aH_2O = 1$. The $P-T$ path (bold continuous line) takes into account the textural observations in the gedrite-bearing granulites. The temperature is overestimated because of the activity of water which is, in reality, lower than unity.

metamorphic assemblages that we selected for $P-T$ path reconstruction use the M_1 peak metamorphism phases, the intermediate paragenesis corresponding to garnet exsolution in Opx, and the M_2 decompressional metamorphic reactions between primary minerals. The prograde history is not accessible because of the chemical homogenization of garnet at high temperature. We combined the composition of the cores of the largest garnet grains with those of the cores of the matrix biotite and other primary minerals such as orthopyroxene or plagioclase, to obtain $P-T$ conditions of the M_1 peak paragenesis. The M_2 retrograde conditions were estimated by using rims of garnet and plagioclase in contact with adjacent secondary biotite, cordierite and orthopyroxene. The M_2' cooling stage was estimated by a later biotite product developed at the expense of orthopyroxene.

Average $P-T$ calculations were obtained using Thermocalc 3.1 (Powell & Holland 1988; Powell *et al.* 1998) with the expanded internally consistent dataset of September 1997. Components activities were estimated using the AX program (T.J.B. Holland, unpublished). Quartz, sillimanite, ilmenite and rutile were assumed to be pure. For each rock, aH_2O was chosen, after iterating on aH_2O values, on the basis of the best fit (χ^2 test results; all quoted error estimates are at the 95% confidence level or 2σ). The aH^2O is additionally constrained by the presence of graphite in several samples. The results of the average $P-T$ calculations are summarized in Table 4.

Peak metamorphism (M_1)

Sillimanite-free orthopyroxene-bearing and orthopyroxene-free quartz-bearing assemblages allow us to calculate average peak temperature and pressure: sample TD38 (garnet–primary reconstituted orthopyroxene–biotite–plagioclase–K-feldspar–quartz–ilmenite–rutile) gives 7.9 ± 1.1 kbar and 863 ± 43 °C with an optimum aH_2O of 0.3; sample 80–128 (garnet–biotite–plagioclase–K-feldspar–quartz–sillimanite–ilmenite–rutile) gives 7.5 ± 1.3 kbar and 855 ± 77 °C with an optimum aH_2O (in graphite-bearing sample) of 0.7 (the results with an $aH_2O < 0.4$ overlap at 2σ uncertainty, as fit values

Table 4. *Summary of P–T estimates*

	Geothermometers (°C)				Geobarometers (kbar)						Thermocalc software Average *P–T*			
	Grt–Bt PL 83	Grt–Opx H 84	Opx–Bt S *et al.* 90	Grt–Crd P *et al.* 85	Grt–Sil–Pl–Qtz NH 81	Grt–Sil–Pl–Qtz KN 88	Grt–Opx–Pl–Qtz NP 82	Grt–Bt–Pl–Qtz H 90 (Mg)	Grt–Bt–Pl–Qtz H 90 (Fe)	GRIPS BL 86	Grt–Crd–Sil–Qtz P & al. 85	aH_2O	*T*	*P*	Best fit
Peak conditions															
Opx-free metapelites	857 ± 45				7.35 ± 0.7	7.8 ± 0.6		7.7 ± 0.9	7.2 ± 1.2	8 ± 0.6					
Opx-bearing metapelites	827 ± 34														
Sil-free metapelites	798 ± 25	855*	850*				8.1 ± 1.2	8.7 ± 0.5	8.5 ± 1.1	8.2 ± 0.8		0.3	863 ± 43	7.9 ± 1.1	0.95
Ged-bearing granulites					7.9 ± 1.2	8.5 ± 0.6				7.2 ± 0.4					
Exsolution conditions															
Sil-free metapelites		812 ± 25	800 ± 33			6.5 ± 1	6.2 ± 1.1			6.8 ± 0.5		0.2	814 ± 38	5.5 ± 1.1	0.71
Retrograde conditions															
Opx-free metapelites	705 ± 35			695 ± 23	4 ± 1.2	4.8 ± 1.1		4.6 ± 1.4	4.2 ± 1.3	6.25 ± 1.3	4.8 ± 1.1				
Secondary Opx-bearing metapelites	610 ± 86	740 ± 25	660 ± 45	705 ± 60	2.9 ± 1.1	3.5 ± 0.9	3.1 ± 1	3 ± 1	2.75 ± 0.9	4.1 ± 1	5.5 ± 1	0.1	731 ± 98	4.3 ± 1.2	1.10
Silfree metapelites	715 ± 32	745 ± 30	705 ± 40	675 ± 25			4.1 ± 1.1	5.2 ± 1.4	4.8 ± 1	6 ± 1		0.1	697 ± 39	4.3 ± 0.5	1.32
Ged-bearing granulites		690 ± 43		670 ± 55	3 ± 1.5	3.1 ± 1.3	3.4 ± 1.2			5.5 ± 0.8	5.3 ± 0.9				

PL 83, Perchuck & Lavrent'eva (1983); H 84, Harley (1984); S *et al.* 90, Sengupta *et al.* (1990); P *et al.* 85, Perchuck *et al.* (1985); NH 81, Newton & Haselton (1981); KN 88, Koziol & Newton (1988); NP 82, Newton & Perkins (1982) H 90, Hoisch (1990); BL 86, Bohlen & Liotta (1986).
*With reconstituted orthopyroxene.

are outside statistical limits; see other calculations in Table 4).

Temperatures were calculated for an assumed pressure of 8 kbar, using the garnet–biotite (Perchuck & Lavrent'eva 1983), garnet–orthopyroxene (Harley 1984) and orthopyroxene–biotite (Sengupta *et al.* 1990) geothermometers. The calculated temperatures are around 857 ± 45 °C, 827 ± 34 °C and 798 ± 25 °C for orthopyroxene-free quartz-bearing metapelites, secondary-orthopyroxene-bearing metapelites and sillimanite-free orthopyroxene-bearing metapelites, respectively, using the calibration of Perchuk & Lavrent'eva (1983). The temperatures calculated using the estimation, by image analysis and microprobe scanning, of the primary orthopyroxene compositions before exsolution are around 865 °C (Grt–Opx: Harley 1984) and 848 °C (Bt–Opx: Sengupta *et al.* 1990).

Pressure estimates were based on the garnet–sillimanite–plagioclase–quartz, garnet–orthopyroxene–plagioclase–quartz, garnet–biotite–plagioclase–quartz and garnet–rutile–ilmenite–plagioclase–quartz assemblages. All these geobarometers give a pressure between 7 and 8.5 kbar. The M_1 granulite-facies event can thus be set at 800–875 °C and 7–8.5 kbar (Fig. 12a).

Decompressional (M_2) and cooling evolution (M_2')

The *P–T* conditions of the exsolutions in orthopyroxene of sillimanite-free metapelites can be also calculated. Orthopyroxene–garnet–plagioclase–biotite–K-feldspar–quartz–ilmenite–rutile assemblage gives 5.5 ± 1.1 kbar and 814 ± 38 °C with $aH_2O = 0.2$ (with best results of average *P–T* of Thermocalc). The later stage is calculated with sample TD38 (sillimanite-free orthopyroxene-bearing metapelites) and sample TD57b (secondary orthopyroxene-bearing metapelites). Sample TD38 contains garnet–orthopyroxene–biotite–plagioclase–spinel–cordierite–quartz–K-feldspar–ilmenite–rutile assemblage and gives 4.3 ± 0.5 kbar and 697 ± 39 °C for an optimum aH_2O of 0.1. Sample TD57b is a metapelite in which garnet displays cracks filled with orthopyroxene–spinel–cordierite–plagioclase; this latter assemblage suggests 4.3 ± 1.2 kbar and 731 ± 98 °C for an

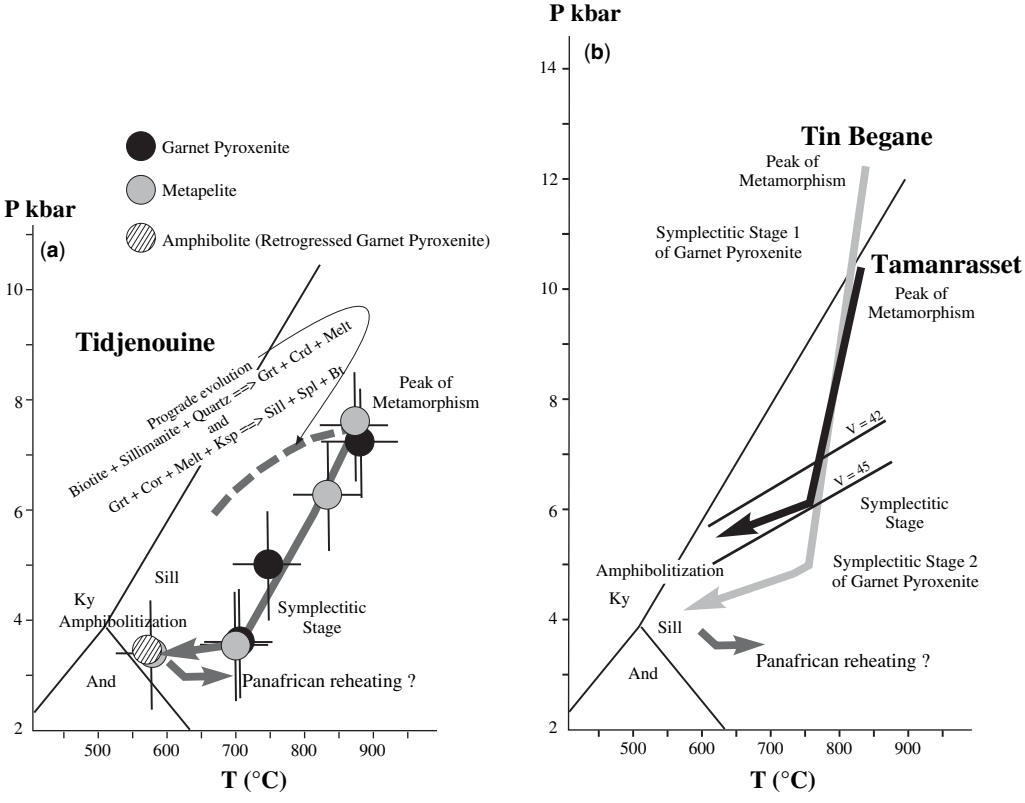

Fig. 12. *P–T* evolution of Tidjenouine metapelites. (**a**) *P–T* path; (**b**) comparison of Tidjenouine metapelites evolution with the metamorphic evolution of Tamanrasset (Ouzegane *et al.* 2001) and Tin Begane (Derridj *et al.* 2003).

optimum aH_2O of 0.1. Results with an $aH_2O > 0.3$ for these two samples show fit values outside statistical limits. Combination of classical geobarometers and geothermometers (Grt–Bt, Grt–Opx, Bt–Opx and Grt–Crd: Table 4) indicates that the later cooling stage occurred at a pressure of 3–4 kbar and temperatures from 745 to 610 °C (from M_2 to M_2'). However, the lowest temperature may correspond to a lower diffusion or to the amphibolitization stage.

These results show a good agreement between the *P–T* conditions obtained from Thermocalc and those obtained from the calibrated geothermometers and geobarometers. The M_2 granulite-facies event can thus be estimated at 700 ± 50 °C and 3–4 kbar (Fig. 12a).

The late M_3 heating metamorphism

The M_2' amphibolite-facies retrogression is evidenced by the appearance of anthophyllite in the gedrite granulites and of cummingtonite and brown–green hornblende in the metabasic rocks. This stage is followed, along the mega-shear zone, by the crystallization of sillimanite in the metapelites and by the breakdown of amphibole, if quartz is present, to orthopyroxene and plagioclase. The recrystallizations are considered as distinct from M_2 and M_2' because: (1) sillimanite crosscuts sharply the former mineral orientation; (2) the assemblages indicate a reheating compared with the M_2' stage at the amphibolite–granulite transition; (3) in contrast to M_2 and M_2', its development is associated spatially with the Pan-African mega-shear zones. This late M_3 phase should have occurred at *c*. 650–700 °C. This temperature and the association with the mega-shear zones suggests that this phase could be linked with the Pan-African batholiths, whose emplacement is also associated with the mega-shear zones, particularly the Anfeg and Tin Amzi batholiths present in the vicinity of the Tidjenouine granulites (Acef *et al.* 2003; Fig. 1c).

Zircon U–Pb ages of the Tidjenouine granulites

Zircons were hand-picked in alcohol from the least magnetic concentrates (1° tilt at full amperage). Selected crystals were then embedded in epoxy resin, ground and polished to expose the internal structure. They were subsequently observed by back-scattered electron (BSE) imaging using a scanning electron microscope (SEM) at the University of Montpellier II. The sample mounts were later used for U–Th–Pb microanalyses using a Lambda Physik COMPex 102 excimer laser generating 15 ns pulses of radiation at a wavelength of 193 nm. For analyses, the laser was coupled to a VG Plasmaquad II ICP-MS and analytical procedures followed those outlined by Bruguier *et al.* (2001) and described in earlier reports (e.g. Neves *et al.* 2006). Analyses where acquired during two analytical sessions where the spot size of the laser beam was 26 and 51 μm. Unknowns were bracketed by measurements of the G91500 zircon standard (Wiedenbeck *et al.* 1995), which were used for mass bias and inter-element fractionation corrections. The calculated bias factors and their associated errors were then added in quadrature to the errors measured on each unknown. Accurate common Pb correction during laser ablation analyses is difficult to achieve, mainly because of the isobaric interference of ^{204}Hg with ^{204}Pb. The contribution of ^{204}Hg to ^{204}Pb was estimated by measuring the ^{202}Hg and assuming a $^{202}Hg/^{204}Hg$ natural isotopic composition of 0.2298. This allows monitoring of the common Pb content of the analysed zircon domain, but corrections often resulted in spurious ages. Analyses yielding ^{204}Pb close to or above the limit of detection were thus rejected, and in Table 5 we report only analyses that were found to contain no common Pb.

Zircons were separated from the Tidjenouine TJ5 granulitic-facies orthogneiss, a sample with a simple mineralogy comprising quartz, K-feldspar, plagioclase, biotite, opaque minerals, zircon and apatite. These zircons typically present an internal structure characterized by three concentric zones (Fig. 13): (1) a central zone that is most often grey and homogeneous in BSE but sometimes has a faint oscillatory zoning (e.g. Zr4, Fig. 13); (2) a first rim, brighter in BSE, with a spongy appearance, containing numerous tiny inclusions of calcite; (3) a second rim, not always developed, which is homogeneous and grey in BSE and has no inclusions. Most grains have rounded terminations but still preserve a prismatic shape, suggesting a metamorphic corrosion of originally magmatic grains. In addition, a few grains are not prismatic and display more simple internal structure (Fig. 13, Zr10). The spongy BSE-bright areas are still zircon and the BSE-dark tiny inclusions are calcite. Thus there has not been a destabilization of a pre-existing zircon, but a syncrystallization of zircon and calcite from a melt. This abundance of calcite in these intermediate zones can be correlated to the granulitic-facies metamorphism: (1) fluid inclusions linked to the granulitic decompression stage in the Tamanrasset area are rich in CO_2 (Ouzegane *et al.* 2001); (2) calcite has been

Table 5. *U–Th–Pb LA-ICP-MS results for zircon grains from Tidjenouine granulite TJ5*

Sample	Pb* (ppm)	U (ppm)	Th (ppm)	Th/U	$^{206}Pb/^{204}Pb$	$^{208}Pb/^{206}Pb$	$^{207}Pb/^{206}Pb$	±(1σ)	$^{207}Pb/^{235}U$	±(1σ)	$^{206}Pb/^{238}U$	±(1σ)	ρ	Apparent ages (Ma) $^{206}Pb/^{238}U$	±(1σ)	$^{207}Pb/^{206}Pb$	±(1σ)	Disc.
Spots on the 2151 Ma discordia																		
li02	140	318	244	0.77	159797	0.215	0.13076	0.00045	6.651	0.153	0.36888	0.00838	0.99	2024	39	2108	6	4.0
li03	135	306	235	0.77	163551	0.218	0.13418	0.00054	7.000	0.160	0.37830	0.00851	0.98	2068	40	2153	7	4.0
li04	30	70	40	0.57	38535	0.159	0.13042	0.00048	6.606	0.170	0.36734	0.00936	0.99	2017	44	2104	6	4.1
li07	143	397	170	0.43	174901	0.125	0.12763	0.00044	5.818	0.144	0.33058	0.00811	0.99	1841	39	2066	6	10.9
li08	120	251	195	0.78	138113	0.217	0.13445	0.00055	7.260	0.163	0.39165	0.00863	0.98	2130	40	2157	7	1.2
li10	112	256	190	0.74	129133	0.213	0.13257	0.00053	6.735	0.079	0.36848	0.00405	0.94	2022	19	2132	7	5.2
li16	55	125	73	0.58	62533	0.161	0.13323	0.00054	7.179	0.135	0.39077	0.00716	0.98	2126	33	2141	7	0.7
li17	83	326	110	0.34	104594	0.134	0.11517	0.00351	3.727	0.271	0.23472	0.01547	0.91	1359	80	1883	55	27.8
li18	81	205	125	0.61	95732	0.169	0.12872	0.00088	6.181	0.085	0.34826	0.00414	0.87	1926	20	2081	12	7.4
li24	52	126	70	0.56	60632	0.158	0.13232	0.00089	6.743	0.095	0.36960	0.00457	0.88	2028	21	2129	12	4.8
qs02	48	219	77	0.35	326906	0.148	0.11281	0.00275	3.086	0.155	0.19842	0.00872	0.87	1167	47	1845	44	36.8
qs03	24	93	24	0.26	220634	0.094	0.11711	0.00067	4.008	0.084	0.24820	0.00501	0.96	1429	26	1913	10	25.3
qs04	85	274	148	0.54	506884	0.187	0.12378	0.00085	4.664	0.142	0.27324	0.00812	0.97	1557	41	2011	12	22.6
qs05	53	123	76	0.62	333740	0.194	0.13127	0.00118	6.735	0.156	0.37210	0.00792	0.92	2039	37	2115	16	3.6
qs07	61	200	74	0.37	400226	0.117	0.12274	0.00052	4.739	0.132	0.28004	0.00772	0.99	1592	39	1996	8	20.3
qs08	45	114	56	0.49	319632	0.170	0.12940	0.00111	6.227	0.102	0.34900	0.00490	0.85	1930	23	2090	15	7.7
qs09	90	204	158	0.78	512480	0.222	0.13427	0.00034	7.258	0.134	0.39205	0.00716	0.99	2132	33	2155	4	1.0
qs10	95	220	158	0.72	599168	0.216	0.13117	0.00079	6.711	0.056	0.37109	0.00216	0.69	2035	10	2114	11	3.7
qs11	55	128	80	0.62	280694	0.187	0.13436	0.00026	7.346	0.204	0.39653	0.01101	1.00	2153	51	2156	3	0.1
qs12	83	193	132	0.68	474308	0.190	0.13120	0.00091	6.731	0.109	0.37208	0.00547	0.90	2039	26	2114	12	3.5
qs15	62	148	90	0.61	418714	0.168	0.13313	0.00067	6.904	0.077	0.37612	0.00378	0.89	2058	18	2140	9	3.8
qs16	47	128	60	0.47	249846	0.146	0.12741	0.00034	5.891	0.068	0.33532	0.00377	0.97	1864	18	2063	5	9.6
qs17	71	191	117	0.61	388996	0.183	0.12971	0.00061	5.931	0.195	0.33162	0.01078	0.99	1846	52	2094	8	11.8
qs19	80	181	104	0.58	470528	0.162	0.13112	0.00104	7.103	0.161	0.39294	0.00836	0.94	2136	39	2113	14	−1.1
qs20	76	178	127	0.71	413632	0.209	0.13150	0.00083	6.797	0.058	0.37486	0.00214	0.67	2052	10	2118	11	3.1
qs22	81	221	115	0.52	513796	0.157	0.13138	0.00207	5.176	0.171	0.28575	0.00917	0.97	1620	46	2116	28	23.4
qs24	87	223	138	0.62	493368	0.186	0.12958	0.00092	6.228	0.145	0.34859	0.00775	0.95	1928	37	2092	12	7.9
qs25	39	130	75	0.58	235016	0.176	0.12503	0.00061	4.729	0.052	0.27429	0.00267	0.89	1563	13	2029	9	23.0
qs27	3	24	1	0.04	30015	0.076	0.09180	0.00190	1.595	0.101	0.12602	0.00755	0.94	765	43	1463	39	47.7
qs28	72	181	112	0.62	435708	0.200	0.13130	0.00144	6.202	0.255	0.34255	0.01356	0.96	1899	65	2115	19	10.2
qs29	59	174	83	0.48	365896	0.163	0.12718	0.00096	5.318	0.226	0.30325	0.01270	0.98	1707	63	2059	13	17.1
qs31	124	309	238	0.77	631400	0.226	0.13247	0.00059	6.238	0.088	0.34155	0.00456	0.95	1894	22	2131	8	11.1
qs32	87	243	151	0.62	460598	0.186	0.12991	0.00209	5.585	0.217	0.31182	0.01102	0.91	1750	54	2097	28	16.6

(*Continued*)

Table 5. *Continued*

Sample	Pb* (ppm)	U (ppm)	Th (ppm)	Th/U	$^{206}Pb/^{204}Pb$	$^{208}Pb/^{206}Pb$	$^{207}Pb/^{206}Pb$	±(1σ)	$^{207}Pb/^{235}U$	±(1σ)	$^{206}Pb/^{238}U$	±(1σ)	ρ	Apparent ages (Ma)				Disc.
														$^{206}Pb/^{238}U$	±(1σ)	$^{207}Pb/^{206}Pb$	±(1σ)	
qs33	41	98	42	0.43	217364	0.118	0.13169	0.00121	6.881	0.136	0.37902	0.00666	0.89	2072	31	2121	16	2.3
qs34	64	274	97	0.35	336960	0.164	0.12129	0.00131	3.652	0.074	0.21839	0.00377	0.85	1273	20	1975	19	35.5
qs35	122	295	199	0.68	560518	0.192	0.13123	0.00052	6.910	0.072	0.38190	0.00373	0.93	2085	18	2115	7	1.4
Spots on the 2062 Ma discordia																		
li01	45	314	42	0.13	65431	0.047	0.07952	0.00069	1.683	0.185	0.15346	0.01682	1.00	920	93	1185	17	22.3
li05	51	230	55	0.24	78852	0.058	0.10386	0.00222	3.179	0.186	0.22198	0.01206	0.93	1292	63	1694	39	23.7
li06	88	743	30	0.04	126845	0.016	0.07834	0.00057	1.326	0.022	0.12274	0.00178	0.89	746	10	1155	14	35.4
li09	36	135	38	0.28	47865	0.083	0.11461	0.00179	4.124	0.202	0.26097	0.01209	0.95	1495	62	1874	28	20.2
li11	79	643	17	0.03	111001	0.015	0.08021	0.00038	1.425	0.028	0.12883	0.00250	0.97	781	14	1202	9	35.0
li12	85	666	19	0.03	115340	0.024	0.08773	0.00042	1.686	0.058	0.13941	0.00472	0.99	841	27	1377	9	38.9
li19	31	130	51	0.39	37315	0.149	0.10696	0.00230	3.289	0.179	0.22299	0.01112	0.92	1298	58	1748	39	25.8
qs06	91	221	145	0.66	521178	0.203	0.12592	0.00097	6.222	0.062	0.35837	0.00229	0.64	1974	11	2042	14	3.3
qs14	8	50	4	0.08	83814	0.069	0.08833	0.00145	2.027	0.038	0.16645	0.00146	0.47	993	8	1390	32	28.6
qs18	73	204	72	0.35	441820	0.113	0.12675	0.00059	5.953	0.091	0.34065	0.00496	0.95	1890	24	2053	8	8.0
qs21	61	199	83	0.42	369426	0.111	0.11877	0.00068	4.679	0.117	0.28573	0.00693	0.97	1620	35	1938	10	16.4
qs23	68	181	32	0.18	450526	0.076	0.12713	0.00093	6.437	0.106	0.36724	0.00542	0.90	2016	25	2059	13	2.1
qs30	72	193	86	0.44	468496	0.131	0.12402	0.00136	5.843	0.227	0.34169	0.01274	0.96	1895	61	2015	19	6.0
Spots on the concordia at 614 Ma																		
li15	10	105	1	0.01	13132	0.006	0.06081	0.00086	0.848	0.052	0.10108	0.00598	0.97	621	35	633	31	1.9
li13	9	102	1	0.01	12645	0.006	0.06032	0.00058	0.836	0.018	0.10052	0.00190	0.89	617	11	615	21	−0.4
li21	8	89	1	0.02	11241	0.006	0.06066	0.00048	0.835	0.017	0.09982	0.00190	0.92	613	11	627	17	2.2
li14	11	120	2	0.01	15700	0.005	0.06004	0.00093	0.826	0.044	0.09982	0.00506	0.96	613	30	605	34	−1.4
qs13	6	65	1	0.01	41346	0.011	0.06146	0.00182	0.831	0.030	0.09801	0.00194	0.56	603	11	655	64	8.0
qs1	5	55	1	0.01	34388	0.018	0.06179	0.00048	0.840	0.018	0.09865	0.00197	0.93	606	12	667	17	9.0

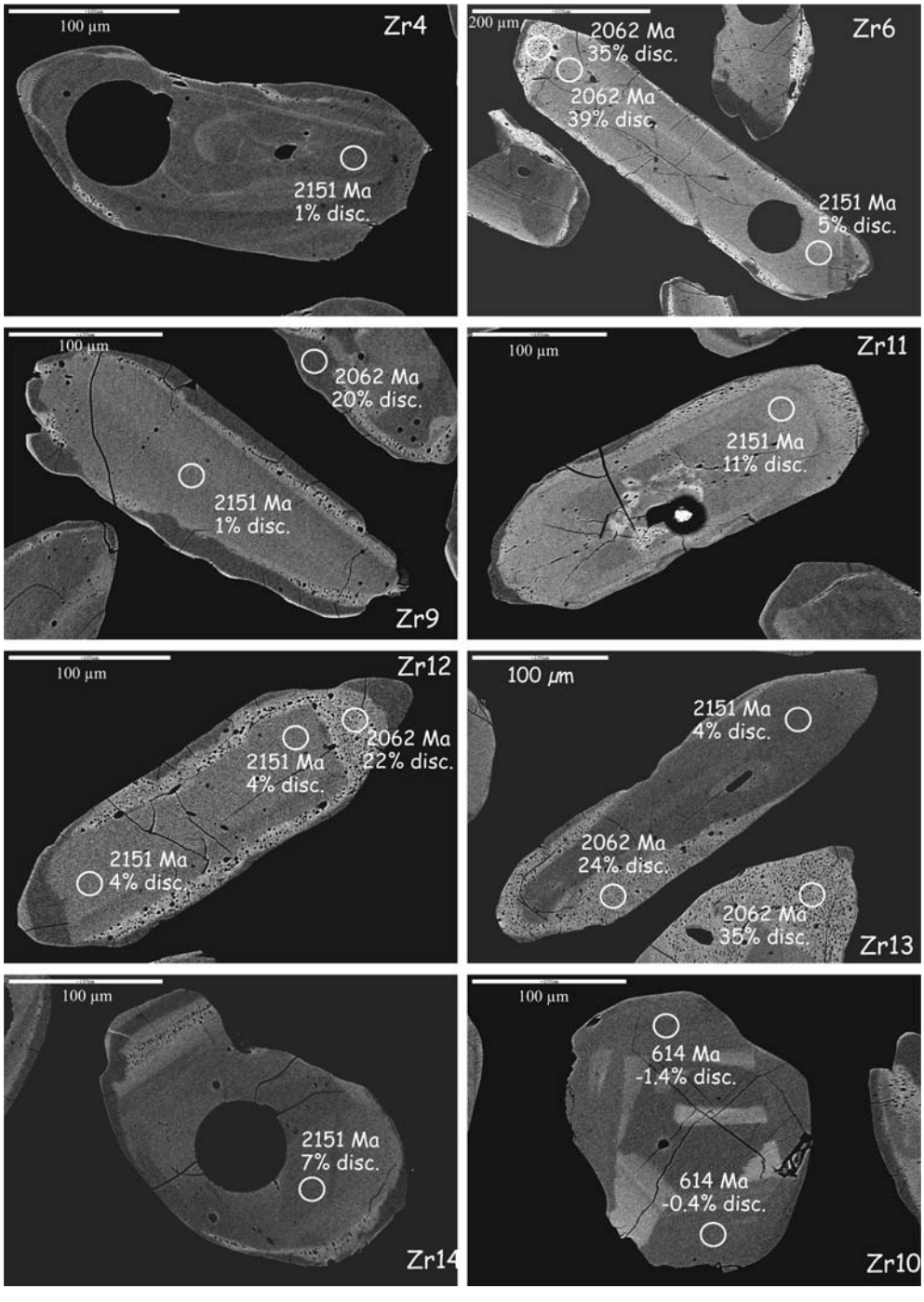

Fig. 13. Texture of the dated Tidjenouine zircon using SEM (back-scattered electrons). White circles indicate the location of spot analyses. Ages indicated are the discordia or concordia ages shown Figure 14. '% disc.' gives the degree of discordance of the considered spot. 'Spongy' areas are made of zircon with tiny inclusions of apatite. In crystal Zr6, there is one spot on a central grey zone with an age of 2062 Ma: this is attributed to the presence of the spongy zone present very close to the spot just below the analysed surface. This is just visible on close inspection of the picture.

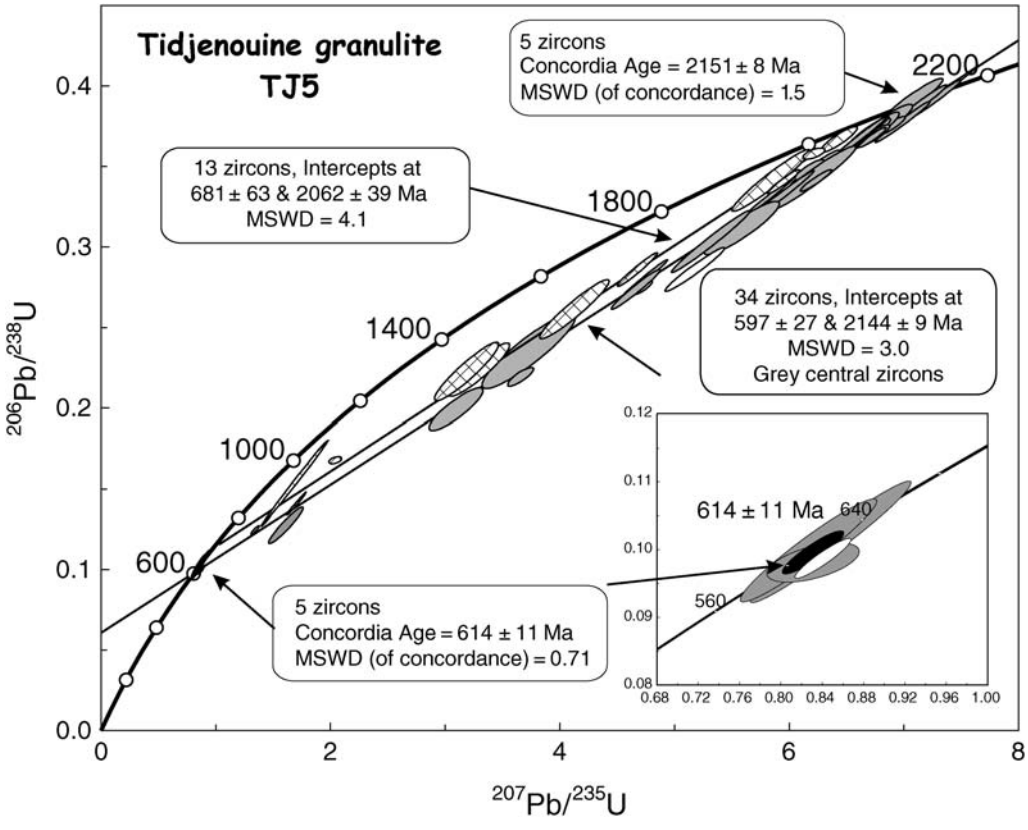

Fig. 14. Zircon U–Pb concordia diagrams showing concordia and discordia ages: the grey ellipses correspond to the zircon grey central zones, the hatched ellipses to the zircon 'spongy' zones; within the inset, the ellipses correspond to single zircons not displaying the corona texture of most of the Tidjenouine zircons (grey: used in the calculation; white: not used (for calculation including that spot, see text); black: result of the concordia age calculation).

described as a granulitic metamorphic phase in the same area (Ouzegane 1981); (3) the presence of Ca-rich minerals (Ca-plagioclase, apatite) in melanosome in the Tidjenouine granulite-facies migmatite suggests that Ca was in excess during the granulitic migmatitization. This means that these inclusion-rich zones should be related to the granulite-facies migmatitic event.

Sixty spots have been analysed on these zircons. They show a broad alignment from *c*. 2100 Ma to *c*. 600 Ma. When considering these results and the relation between ages and the different zircon domains (Fig. 14), the following patterns arise.

(1) Thirty-four spots in central grey zones define a discordia line with an upper intercept of 2144 ± 9 Ma and a lower intercept of 597 ± 27 Ma (2σ, MSWD = 1.5). Among these analyses, five concordant spots provide a slightly older but consistent age of 2151 ± 8 Ma (2σ, five zircons, MSWD = 1.5). We consider this last age as the best estimate for the crystallization of these central zones. Th/U ratios of this group vary between 0.78 and 0.43 for spots with $^{206}Pb/^{238}U$ ages above 1700 Ma, those with younger $^{206}Pb/^{238}U$ ages having ratios between 0.58 and 0.26.

(2) Thirteen spots in spongy intermediate zones define a discordia line with an upper intercept of 2062 ± 39 Ma and a lower intercept of 681 ± 63 Ma (2σ, MSWD = 4.1); there are no true concordant spots in this group but four spots have only a slight discordance below 8%: their mean $^{207}Pb/^{206}Pb$ age is 2049 ± 22 Ma; Th/U ratios of this group vary between 0.66 and 0.24 for spots with $^{206}Pb/^{238}U$ ages above 1200 Ma, those with $^{206}Pb/^{238}U$ ages below 1000 Ma having ratios between 0.03 and 0.13. We note that the U and Pb concentrations in these analyses are not significantly different from those of the first group (Table 5), indicating that the calcite inclusions present in these zones do not interfere in these analyses, as we would expect.

(3) Five spots obtained in the non-prismatic core-free zircons are concordant close to the previous discordia lower intercepts and a sixth one is nearly concordant. Our best estimate for this batch of analyses is 614 ± 11 Ma (five zircons, MSWD = 0.71). Their Th/U ratios are very low, between 0.01 and 0.02. The outer rims displayed by some zircons were too thin to be analysed by the laser ablation technique but we propose the hypothesis that a similar Pan-African age would have been acquired on these zones. Finally two spots are slightly below the two discordias and have not been included in the age calculations.

The oldest age of 2151 ± 8 Ma has been determined on central parts of the grains, some of which are zoned and characteristic of a magmatic crystallization. This age is thus attributed to the magmatic protolith of the granulite. The slightly younger age of 2062 ± 39 Ma is questionable, as it has been calculated from discordant analyses sampling the intermediate coronas linked to the granulitic migmatitic event (M_1 and M_2 phase). The location of these data points on the left of the *c*. 2.15–0.60 Ga discordia line indicates that these zones have undergone U–Pb disturbances, at some times in the past, between these two ages. The limited degree of discordance of some of these analyses (<10%) is taken as evidence for a Palaeoproterozoic age for this event. This would imply that both the prograde M_1 and retrograde M_2 metamorphic phases are Eburnean in age and most probably correspond to one metamorphic path. A younger age (i.e. Neoproterozoic) for the granulitic event cannot be strictly ruled out in the absence of concordant analyses but is unlikely: in this case, the spots acquired on the intermediate zones should lie on a discordia line pointing to *c*. 2.15 Ga and not as much to the left. The rare independent crystals unzoned and unaffected by the reaction coronas are dated at 614 ± 11 Ma, an age that can probably be applied to the thin external rims of most zircons. This age corresponds to that of the intrusion of the neighbouring granitic batholiths such as the Anfeg batholith (608 ± 7 Ma; U–Pb zircon, Bertrand *et al.* 1986, recalculated by Liégeois *et al.* 2003) and thus to the M_3 thermal metamorphic phase, which is thus Pan-African in age. The fact that this phase was the most effective in lowering the Th/U ratio indicates that during the Pan-African M_3 metamorphism, only solid-state reactions occurred, whereas melts were produced during the Eburnean M_1–M_2 granulite-facies migmatitic event, the lowering of the Th/U ratio being favoured by metamorphic fluids (Williams *et al.* 1996), which probably eased the exchange of Th between zircon and minerals such as monazite.

Discussion and conclusion

In several areas of the Laouni terrane, observed granulitic formations are commonly associated with an important migmatitic event. The textural relationships and the P–T estimates suggest that the beginning and maintenance of melt production occurred during the prograde metamorphic evolution (M_1) culminating at 850 °C and 7.5 kbar. A large part of the retrograde evolution (M_2) down to 700 °C and 4 kbar, also occurred under granulite-facies conditions: the presence of early, strongly restitic granulites (corundum metapelites earlier than the garnet–sillimanite–biotite metamorphic peak) indicates that migmatitization was already important before the M_1 climax and some melt was also produced during the late breakdown of biotite (M_2). The M_2 stage evolved eventually to an M_2' phase in the amphibolite facies at 600 °C, which is evidenced by some late minerals such as anthophyllite, secondary biotite and cummingtonite, depending on the rock type. This granulitic metamorphism is Eburnean (2062 ± 39 Ma). This clockwise retrograde P–T segment is similar to that constructed using a variety of different rock types (metapelitic and metabasic rocks) from the basement of the Laouni terrane (Ouzegane *et al.* 2001; Bendaoud *et al.* 2003; Derridj *et al.* 2003). During this evolution $a\mathrm{H_2O}$ generally decreased, probably because of absorption of H_2O in anatectic melts, preserving most of the granulite-facies parageneses (M_2' is local).

Our petrological and thermobarometric study indicates a clockwise P–T path marked by a decompression stage generating spectacular coronitic and symplectitic textures in both the para- and ortho-derived metamorphic units. The succession of parageneses during this decompression depends on the chemical composition of the rocks. In Tidjenouine, the metapelites and the microdomains rich in Si and Mg are characterized by the appearance of an orthopyroxene–cordierite association at the expense of garnet, quartz and biotite, in the absence of sillimanite. On the other hand, the metapelites and the microdomains rich in Al and Fe display the spinel–cordierite assemblage, without orthopyroxene, following the destabilization of garnet, sillimanite and biotite. The occurrence of sillimanite inclusions in the core of primary garnet in quartz-bearing metapelites confirms that this mineral was present during the prograde stage.

The peak pressures obtained at Tamanrasset (10 kbar: Ouzegane *et al.* 2001) and at Tin Begane (12 kbar: Derridj *et al.* 2003) are higher than those obtained in the study area (7–8 kbar). This can be related to different exposed crustal levels (Bendaoud *et al.* 2004). Coupled with the observation of the abundance of often subhorizontal

shear zones, this suggests that the LATEA microcontinent is composed of a series of Eburnean nappes, probably resulting from a collisional orogeny. It is thus possible that the shear zones interpreted as Pan-African in age (Bertrand *et al.* 1986) were initiated during the Eburnean orogeny and reactivated during the Pan-African orogeny. More work is needed to assess this hypothesis. The age of the protolith of the dated sample (2151 ± 8 Ma) is thus probably related to a pre-collisional event such as a subduction regime. No Archaean age is recorded here as in the other regions of the southern LATEA (Bertrand *et al.* 1986; Barbey *et al.* 1989); Archaean ages are currently only known in the Gour Oumelalen region (NE LATEA; Peucat *et al.* 2003; Fig. 1). This could suggest the existence of an Archaean continent to the NE involved to the SW in a collisional orogeny with a Palaeoproterozoic terrane, but more geochronological, metamorphic and geochemical data are needed to proceed in this interpretation. We can point that the Eburnean granulitic metamorphism in the Archaean Gour Oumelalen area is younger (*c.* 1900 Ma; Peucat *et al.* 2003) than in SW LATEA (*c.* 2100 Ma; Barbey *et al.* 1989; this study). The geodynamic understanding of the Eburnean evolution of Hoggar is still in its infancy.

The age of 614 ± 11 Ma obtained on single unzoned zircons and the large discordance of many Eburnean zircons indicate that the effect of the Pan-African orogeny was important in LATEA although the Eburnean granulite-facies parageneses are well preserved. Similar ages have been obtained on the Telohat migmatites (609 ± 17 Ma; U–Pb zircon lower intercept; Barbey *et al.* 1989). The Pan-African event is marked by the M_3 thermal metamorphism (650 °C; 3–4 kbar) that led to the destabilization of the amphibole in the metabasic rocks and probably of the biotite in the metapelites, and allowed the crystallization of a new generation of sillimanite not linked to the M_1–M_2 metamorphic phase, as postulated by Caby (2003). The M_3 metamorphism is synchronous with the large Pan-African batholiths such as the Anfeg batholith (608 ± 7 Ma: U–Pb zircon, Bertrand *et al.* 1986, recalculated by Liégeois *et al.* 2003); these in turn are synchronous with the development of the large shear zones characteristic of the Tuareg shield (Fig. 1). These batholiths are rooted in the subvertical major shear zones and were emplaced as sheets along reactivated pre-existing subhorizontal shear zones (Acef *et al.* 2003; Liégeois *et al.* 2003). We can here confirm the pre-existence of these subhorizontal shear zones, to which we attribute an initial Eburnean age on the basis of the above petrological results linked to the dated *c.* 2060 Ma granulitic-facies metamorphism. True dating of these shear zones remains to be done.

These findings shed light on the LATEA Pan-African metacratonic evolution (Liégeois *et al.* 2003): the LATEA microcontinent was mainly built during the Eburnean orogeny, which generated a regional granulite-facies metamorphism, and became a craton by lithospheric thickening (Black & Liégeois 1993) during the Mesoproterozoic, a quiet period for LATEA (no Mesoproterozoic events are recorded in central Hoggar) as for most of West Africa. This rigid cratonic behaviour allowed LATEA to become amalgamated with several Neoproterozoic island arcs (Liégeois *et al.* 2003): the Iskel terrane at 870–850 Ma (Caby *et al.* 1982), and the Tin Begane unit at *c.* 685 Ma (Liégeois *et al.* 2003) among others, which are not yet dated. These accretion events are not recorded in the Tidjenouine granulites. The main Pan-African orogenic phase is characterized by large horizontal movements along mega-shear zones and the intrusion of granitoid batholiths in the 620–580 Ma age range (Bertrand *et al.* 1986; Caby & Andreopoulos-Renaud 1989; Black *et al.* 1994; Liégeois *et al.* 1994, 2003). This phase dismembered the LATEA craton and heat transfer was caused by the magmas rising along the shear zones, although many of the cratonic features were preserved, including the Eburnean granulitic paragenesis and probably many Eburnean structures, although they were slightly to strongly reworked. This corresponds to the notion of metacraton (Abdelsalam *et al.* 2002) that can be applied to LATEA (Liégeois *et al.* 2003). Taking into account the relatively small area of LATEA, we can suggest that it belonged, before the Pan-African orogeny, to a larger craton probably constituting its margin. Whether LATEA represents the former eastern boundary of the West African craton or the western boundary of the Saharan craton is still a matter of debate. The Tidjenouine area demonstrates the complexity of metacratonic areas that result from the interplay of two orogenies on a rigid block. This is the reason why metacratonic areas are most often not well understood and are probably now among the most fascinating regions to study with modern techniques.

We warmly thank G. Rebay and P. Goncalves for their reviews, which significantly improved the final version of the manuscript. Lively discussions with R. Caby on the Eburnean v. Pan-African effects in Hoggar were appreciated. We thank N. Ennih for his editorial comments. This work was supported by the TASSILI 05

MDU 653 project 'Imagerie tridimentionnelle et évolution spatio-temporelle du Hoggar' and by the NATO grant EST/CLE 979766 and CNRS PICS project 'Architecture lithosphérique et dynamique du manteau sous le Hoggar'. We are also extremely grateful to ORGM and OPNA for logistic support during fieldwork.

References

ABDELSALAM, M., LIÉGEOIS, J. P. & STERN, R. J. 2002. The Saharan metacraton. *Journal of African Earth Science*, **34**, 119–136.

ACEF, K., LIÉGEOIS, J. P., OUABADI, A. & LATOUCHE, L. 2003. The Anfeg post-collisional Pan-African high-K calc-alkaline batholith (Central Hoggar, Algeria), result of the LATEA microcontinent metacratonisation. *Journal of African Earth Sciences*, **37**, 95–311.

ADJERID, Z., OUZEGANE, K., GODARD, G. & KIENAST, J. R. 2008. First report of ultrahigh- temperature sapphirine spinel quartz and orthopyroxene + spinel + quartz parageneses discovered in Al–Mg granulites from the Khanfous area (In Ouzzal metacraton, Hoggar, Algeria). *In*: ENNIH, N. & LIÉGEOIS, J.-P. (eds) *The Boundaries of the West African Craton* Geological Society, London, Special Publications, **297**, 147–167.

BARBEY, P., BERTRAND, J. M., ANGOUA, S. & DAUTEL, D. 1989. Petrology and U/Pb geochronology of the Telohat migmatites, Aleksod, Central Hoggar, Algeria. *Contributions to Mineralogy and Petrology*, **101**, 207–219.

BENDAOUD, A., OUZEGANE, K. & KIENAST, J. R. 2003. Textures and phase relationships in ferrous granulites from Tidjenouine (Hoggar, Algeria): fayalite–ferrossilite–quartz secondary assemblage. *Journal of African Earth Sciences*, **37**, 241–255.

BENDAOUD, A., DERRIDJ, A., OUZEGANE, K. & KIENAST, J. R. 2004. Granulites of the Laouni terrane, (Tamanrasset, Tidjenouine, Tin Begane). *Journal of African Earth Sciences*, **39**, 187–192.

BENYAHIA, O., HADDOUM, H., OUZEGANE, K., BENDAOUD, A., DJEMAI, S. & KIENAST, J.-R. 2005. Fonctionnement et rôle des méga zones de cisaillement dans la structuration du métacraton éburnéen du LATEA au panafricain puis au phanérozoïque (région de Tamanrasset, Hoggar, Algérie). *African Geosciences Review*, **12**, 261–274.

BERTRAND, J.-M. & JARDIM DE SÁ, E. F. 1990. Where are the Eburnean–Transamazonian collisional belts? *Canadian Journal of Earth Sciences*, **27**, 1382–1393.

BERTRAND, J. M., MICHARD, A., BOULLIER, A. M. & DAUTEL, D. 1986. Structure and U/Pb geochronology of Central Hoggar (Algeria): a reappraisal of its Pan-African evolution. *Tectonics*, **5**, 955–972.

BLACK, R. & LIÉGEOIS, J. P. 1993. Cratons, mobile belts, alkaline rocks and continental lithospheric mantle: the Pan-African testimony. *Journal of the Geological Society, London*, **150**, 89–98.

BLACK, R., LATOUCHE, L., LIÉGEOIS, J. P., CABY, R. & BERTRAND, J. M. 1994. Pan-African displaced terranes in the Tuareg shield (central Sahara). *Geology*, **22**, 641–644.

BOHLEN, S. R. & LIOTTA, J. J. 1986. A barometer for garnet amphibolites and granulites. *Journal of Petrology*, **27**, 1025–1034.

BRUGUIER, O., TELOUK, P., COCHERIE, A., FOUILLAC, A. M. & ALBARÈDE, F. 2001. Evaluation of Pb–Pb and U–Pb laser ablation ICP-MS zircon dating using matrix-matched calibration samples with a frequency quadrupled (266 nm) Nd:YAG laser. *Geostandards Newsletter*, **25**, 361–373.

CABY, R. 2003. Terrane assembly and geodynamic evolution of central–western Hoggar: a synthesis. *Journal of African Earth Sciences*, **37**, 133–159.

CABY, R. & ANDREOPOULOS-RENAUD, U. 1989. Age U–Pb à 620 Ma d'un pluton synorogénique de l'Adrar des Iforas (Mali). conséquences pour l'âge de la phase majeure de l'orogène pan-africaine. *Comptes Rendus de l'Académie des Sciences*, **308**, 307–314.

CABY, R., ANDREOPOULOS-RENAUD, U. & GRAVELLE, M. 1982. Cadre géologique et géochronologique U/Pb sur zircon des batholites précoces dans le segment pan-africain du Hoggar central (Algérie). *Bulletin de la Société Géologique de France*, **24**, 677–684.

CZAMANSKE, G. D. & WONES, D. R. 1973. Oxidation during magmatic differentiation, Finnmarka Complex, Oslo area, Norway. II. The mafic silicates. *Journal of Petrology*, **14**, 349–380.

DERRIDJ, A., OUZEGANE, K., KIENAST, J. R. & BELHAÏ , D. 2003. P–T–X evolution in garnet pyroxenites from Tin Begane (Central Hoggar, Algeria). *Journal of African Earth Sciences*, **37**, 257–268.

HANSON, G. N. 1989. An approach to trace element modeling using a simple igneous system as an example. *In*: LIPIN, R. B. & MCKAY, G. A. (eds) *The Geology and Geochemistry of Rare Earth Elements*. Mineralogical Society of America, Reviews in Mineralogy, **21**, 79–97.

HARLEY, S. L. 1984. An experimental study of the partitioning of Fe and Mg between garnet and orthopyroxene. *Contributions to Mineralogy and Petrology*, **86**, 359–373.

HARLEY, S. L. 1989. The origins of granulites: a metamorphic perspective. *Geological Magazine*, **126**, 215–247.

HOISCH, T. D. 1990. Empirical calibration of six geobarometers for the mineral assemblage quartz + muscovite + biotite + plagioclase + garnet. *Contributions to Mineralogy and Petrology*, **104**, 225–234.

HOLLAND, T. J. B. & POWELL, R. 1990. An enlarged and updated internally consistent thermodynamic dataset with uncertainties and correlations: the system K_2O–Na_2O–CaO–MgO–FeO–Fe_2O_3–Al_2O_3–TiO_2–SiO_2–C–H–O. *Journal of Metamorphic Geology*, **8**, 89–124.

KOZIOL, A. M. & NEWTON, R. C. 1988. Redetermination of the anorthite breakdown reaction and improvement of the plagioclase–garnet–Al_2SiO_5–quartz barometer. *American Mineralogist*, **73**, 216–223.

LEAKE, B. E., WOOLLEY, A. R. & BIRCH, W. D. *et al*. 1997. Nomenclature of amphiboles. *Canadian Mineralogist*, **9**, 623–651.

LIÉGEOIS, J. P., BLACK, R., NAVEZ, J. & LATOUCHE, L. 1994. Early and late Pan-African orogenies in the Aïr assembly of terranes (Tuareg shield, Niger). *Precambrian Research*, **67**, 59–88.

LIÉGEOIS, J. P., LATOUCHE, L., BOUGHRARA, M., NAVEZ, J. & GUIRAUD, M. 2003. The LATEA metacraton (Central Hoggar, Tuareg shield, Algeria): behaviour of an old passive margin during the Pan-African orogeny. *Journal of African Earth Sciences*, **37**, 161–190.

NEVES, S., BRUGUIER, O., VAUCHEZ, A., BOSCH, D., RANGEL DA SILVA, J. M. & MARIANO, G. 2006. Timing of crust formation, deposition of supracrustal sequences, and Transamazonian and Brasiliano metamorphism in the East Pernambuco belt (central domain, Borborema Province, NE Brazil): implications for western Gondwana assembly. *Precambrian Research*, **149**, 197–216.

NEWTON, R. C. & HASELTON, H. T. 1981. Thermodynamics of the garnet–plagioclase–Al_2SiO_5–quartz geobarometer. *In*: NEWTON, R. C., NAVROTSKY, A. & WOOD, B. J. (eds) *Thermodynamics of Minerals and Melts*. Springer-Verlag, New York, 131–147.

NEWTON, R. C. & PERKINS, D. I. 1982. Thermodynamic calibration of geobarometers based on assemblages garnet–plagioclase–orthopyroxene (clinopyroxene)–quartz. *American Mineralogist*, **67**, 203–222.

OUZEGANE, K. 1981. *Le métamorphisme polyphasé granulitique de la region de Tamanrasset (Hoggar central)*. Thesé de 3éme cycle, Université, Paris VII, France.

OUZEGANE, K. & BOUMAZA, S. 1996. An example of ultrahigh-temperature metamorphism: orthopyroxene–sillimanite–garnet, sapphirine–quartz and spinel-quartz parageneses in Al–Mg granulites from In Hihaou, In Ouzzal, Hoggar. *Journal of Metamorphic Geology*, **14**, 693–708.

OUZEGANE, K., DJEMAI, S. & GUIRAUD, M. 1996. Gedrite garnet sillimanite bearing granulites from Amesmessa area, south In Ouzzal, Hoggar, Algeria. *Journal of Metamorphic Geology*, **14**, 739–753.

OUZEGANE, K., BENDAOUD, A., KIENAST, J. R. & TOURET, J. L. R. 2001. Pressure–temperature–fluid evolution in the Eburnean metabasites and metapelites from Tamanrasset (Hoggar, Algeria). *Journal of Geology*, **109**, 247–263.

OUZEGANE, K., KIENAST, J. R., BENDAOUD, A. & DRARENI, A. 2003. A review of Archaean and Paleoproterozoic evolution of the In Ouzzal granulitic terrane (Western Hoggar, Algeria). *Journal of African Earth Sciences*, **37**, 207–227.

PERCHUK, L. L. & LAVRENT'EVA, I. V. 1983. Experimental investigation of exchange equilibria in the system cordierite–garnet–biotite. *In*: SAXENA, S. K. (ed.) *Kinetics and Equilibrium in Mineral Reactions.* Advances in Physical Geochemistry, **3**, 199–239.

PERCHUK, L. L., ARANOVICH, L. Y. & PODLESSKII, K. K. *et al*. 1985. Precambrian granulites of the Aldan shield, eastern Siberia, USSR. *Journal of Metamorphic Geology*, **3**, 265–310.

PEUCAT, J. J., DRARENI, A., LATOUCHE, L., DELOULE, E. & VIDAL, P. 2003. U–Pb zircon (TIMS and SIMS) and Sm–Nd whole-rock geochronology of the Gour Oumelalen granulitic basement, Hoggar massif, Tuareg shield, Algeria. *Journal of African Earth Sciences*, **37**, 229–239.

POWELL, R. & HOLLAND, T. J. B. 1988. An internally consistent data set with uncertainties and correlations: 3. Applications to geobarometry worked examples and a computer program. *Journal of Metamorphic Geology*, **6**, 173–204.

POWELL, R., HOLLAND, T. J. B. & WORLEY, B. 1998. Calculating phase diagrams involving solid solutions via nonlinear equations, with examples using THERMOCALC. *Journal of Metamorphic Geology*, **16**, 577–588.

ROBINSON, P., ROSS, M. & JAFFE, H. W. 1971. Composition of the anthophyllite–gedrite series: comparisons of gedrite–hornblende and the anthophyllite–gedrite solvus. *American Mineralogist*, **56**, 1005–1041.

SENGUPTA, P., DASGUPTA, S., BHATTACHARYA, P. K. & MUKHERJEE, M. 1990. An orthopyroxene–biotite geothermometer and its application in crustal granulites and mantle-derived rocks. *Journal of Metamorphic Geology*, **8**, 191–197.

SPEAR, F. S. 1980. The gedrite–anthoplyllite solvus and the composition limits of orthoamphibole from the Post Pond volcanics, Vermont. *American Mineralogist*, **65**, 1103–1118.

SUN, S. S. & MCDONOUGH, W. F., 1989. Chemical and isotopic systematics of oceanic basalts: implications for mantle composition and processes. *In*: SAUNDERS, A. D. & NORRY, M. J. (eds) *Magmatism in the Ocean Basins*. Geological Society, London, Special Publications, **42**, 313–345.

TAYLOR, S. R. & MCLENNAN, S. M. 1985. *The Continental Crust: its Composition and Evolution*. Blackwell, Oxford.

WIEDENBECK, M., ALLÉ, P., CORFU, F., GRIFFIN, W. L. & MEIER, M. 1995. Three natural zircon standards for U–Th–Pb, Lu–Hf, trace element and REE analyses. *Geostandards Newsletter*, **19**, 1–23.

WILLIAM, I. S., BUICK, I. S. & CARTWRIGHT, I. 1996. An extended episode of early Mesoproterozoic metamorphic fluid flow in the Reynold Range, central Australia. *Journal of Metamorphic Geology*, **14**, 29–47.